Various lithospheric deformation patterns derived from rheological contrasts between continental terranes: Insights from 2-D numerical simulations

Renxian Xie[1, 2], Lin Chen[3], Jason P. Morgan[2], Yongshun John Chen[2*]

[1]School of Transportation Engineering, East China Jiaotong University, Nanchang, 330013, China

[2]Department of Ocean Science and Engineering, Southern University of Science and Technology, Shenzhen, 518055, China

[3]State Key Laboratory of Lithospheric Evolution, Institute of Geology and Geophysics, Chinese Academy of Sciences, Beijing, 100029, China

Correspondence to: Yongshun John Chen (johnyc@sustech.edu.cn)

Abstract. Continents are formed by the amalgamation of numerous micro-terranes and island arcs, so they have spatially varying lithosphere strengths. The Crème brûlée (CB) model and the Jelly sandwich (JS) model have been commonly used to describe continental lithosphere strength-depth variations. Depending on the strength of continental lower crust, the CB and JS models can be further subdivided into two subclasses, in which the I subclass (CB-I and JS-I) and II subclass (CB-II and JS-II) respectively have a strong or weak lower crust. During continental collision, lithosphere deformation is the byproduct of the comprehensive interaction of multiple terranes. Here we used 2-D thermo-mechanical numerical models that contain three continental terranes to systematically explore the effects of terranes with various strengths on continental deformation, and studied the effects of different rheological assumptions ~~on~~ terrane deformation. We f~~in~~ound four types of lithosphere deformation patterns: collision, subduction, thickening and delamination, and replacement. ~~Lithosphere structures, especially local pre-existing weaknesses, also have nonnegligible influences on lithosphere deformation.~~ These simulation patterns are seen in observed deformation patterns and structures in East Asia, suggesting they are likely to be naturally occurring modes of intracontinental orogenesis.

1. Introduction

Continents have undergone multiple break-up and assembly events during the past ~2 billion years, with the assembly events often being associated with the accretion and deformation of numerous micro-terranes (Mitchell et al., 2021). Accreted terranes have different ages ranging from ~3500 – 3000

29 Ma to 50 – 0 Ma, and diverse compositions and structures linked to their diverse continental, arc, or

30 oceanic origin, which often leads to them having distinct initial lithospheric thicknesses and strengths

31 (Artemieva, 2006; Audet and Bürgmann, 2011; Pasyanos et al., 2014; Morgan and Vannucchi, 2022).

32 The lithosphere of ancient continental terranes like cratons are usually thick and strong, while younger

33 lithosphere of continental margins and tectonically active regions is thin and weak (Audet and

34 Bürgmann, 2011; Burov, 2011), and deeply buried former oceanic fragments can have temperature and

35 strengths that vary over ~0.5 Gyr timescale (Morgan and Vannucchi, 2022).

36 Continental lithosphere strength conventionally been represented by two prevailing rheology models

37 —the Crème brûlée (CB) and the Jelly sandwich (JS) idealizations (Chen and Molnar, 1983; Jackson,

38 2002; Burov and Watts, 2006; Bürgmann and Dresen, 2008; Burov, 2011). The Crème brûlée scenario

39 suggests that lithosphere strength resides entirely in the crust, with the lithospheric mantle being much

40 weaker (with this strength contrast being the explanation for why little seismicity is typically seen in

41 the continental mantle, despite rock-mechanics arguments that it should usually be stronger than its

42 overlying crust). In contrast, the Jelly sandwich model is based on conventional rock mechanics

43 arguments which imply that in general the continental middle and lower crust should be weaker than

44 overlying cooler upper crust and underlying further-from-solidus lithospheric mantle (Figure 1a). The

45 rheology of the continental lower crust can also differ strongly in different continental terranes due to

46 the varieties in composition, temperature, water content, stress, and tectonic environment (Bürgmann

47 and Dresen, 2008; Hacker et al., 2015; Morgan and Vannucchi, 2022). Therefore, the CB and JS

48 conceptualizations can be further subdivided into CB-I and CB-II, JS-I, and JS-II subclasses that reflect

49 potentially variable strengths of the lower crust: CB-I and JS-I, CB-II and JS-II have strong and weak

50 continental lower crust, respectively (Fig. 1a). Observations in Eastern Asia show a wide variability in

51 terrane deformation styles that argue for the potential feasibility of all four of these rheological models

52 (Figure 1b).

53 Several previous numerical modelling studies have discussed the effects of rheological contrasts

54 between terranes in lithosphere deformation in a collisional system. Studies containing two terranes

55 have explored contrasts in crustal rheology, and found that this can greatly change the morphology, size

56 and deep lithosphere structure of collisional orogenic belt (Chen, 2021; Chen et al., 2017; Cook and

57 Royden, 2008; Faccenda et al., 2008; Sun and Liu, 2018; Vogt et al., 2018; Xie et al., 2021). Strong

58 crust also has the potential to protect its underlying lithospheric mantle from deformation and

destruction (Heron and Pysklywec, 2016). Studies containing three or more terranes in their models have usually focused on the middle terrane which can play a crucial role in lithosphere deformation in a collisional system (Kelly et al., 2016, 2020; Li et al., 2016; Huangfu et al., 2018, 2022; Sun and Liu, 2018; Xie et al., 2023). A weak middle terrane is easy to be thickened, to the point where eventually its lithospheric mantle can be delaminated from the crust; while a moderate-strength middle terrane can induce far-field orogenesis; and a strong middle terrane may prevent propagation of deformation and facilitate underthrusting of the advancing terrane. In addition, some studies have also stressed the importance of local pre-existing weak zones which can change the order and style of lithosphere deformation (Chen et al., 2020; Heron et al., 2016; Sokoutis and Willingshofer, 2011; Xie et al., 2021).

In modern Asia, tLhe large-scale Alpine Himalaya continental collisional system often involves the multiple units of an indenting terrane, a middle terrane, and far-end backwall terranes. These terranes have The different lithosphere rheologies and thicknesses, and theyof these terranes collectively contribute to several styles of continental deformation (Artemieva, 2006; Audet and Bürgmann, 2011; Pasyanos et al., 2014; Morgan and Vannucchi, 2022). Here, we use a 2-D thermo-mechanical numerical modeling method to systematically study the effects of terranes with various rheological properties on continental deformation. Our numerical models simulate a continent-continent collisional system that contains three continental terranes. They explores the effects of four groups of lithosphere deformation patterns linked to the four rheological idealizations of CB-I, CB-II, JS-I, and JS-II applied to each terrane. We will summarize the rheological features for each deformation pattern, and then apply the simulations to better understand ongoing and past deformation histories of various orogenic belts in the global, especially preserved in eastern EurasiaAsia, such as the eastern Tien Shan orogenic belt, the Tibetan Plateau and the Early Paleozoic Orogen in Southeastern China.

2. Numerical modelling method and model setup

2.1. Numerical modelling method

Our thermo-mechanical models were performed with the I2VIS code of Gerya and Yuen (2003), previously used in Xie et al. (2021, 2023). This code combines finite differences with marker-in-cell techniques to solve the mass, momentum, and energy conservation equations for incompressible flow. It incorporates the non-Newtonian visco-plastic rheologies for the lithosphere, as well as the possibility

87 to include parameterizations of the effects of surface processes like sedimentation and erosion.

88 **2.1.1. Governing equations**

89 The mass conservation equation for incompressible flow is:

90
$$\frac{\partial v_x}{\partial x} + \frac{\partial v_y}{\partial y} = 0 \,,$$
(1)

91 The momentum conservation equations (Stokes equations) are:

92
$$\frac{\partial \sigma'_{xx}}{\partial x} + \frac{\partial \sigma'_{xy}}{\partial y} = \frac{\partial P}{\partial x}$$
$$\frac{\partial \sigma'_{yy}}{\partial y} + \frac{\partial \sigma'_{xy}}{\partial x} = \frac{\partial P}{\partial y} - g\rho$$
(2)

93 The energy (heat) conservation equation is:

94
$$\rho C_p \frac{DT}{Dt} = -\frac{\partial q_x}{\partial x} - \frac{\partial q_y}{\partial y} + H_r + H_s + H_a + H_L$$
$$q_x = -k\frac{\partial T}{\partial x}$$
$$q_y = -k\frac{\partial T}{\partial y}$$
$$H_a = T\alpha\frac{DP}{Dt}$$
$$H_s = \sigma'_{xx}\dot{\varepsilon}_{xx} + \sigma'_{yy}\dot{\varepsilon}_{yy} + 2\sigma'_{xy}\dot{\varepsilon}_{xy}$$
(3)

95 where x and y represent the horizontal and vertical coordinate directions, and v_x and v_y are the

96 corresponding velocity components, respectively. σ'_{ij} and $\dot{\varepsilon}_{ij}$ ($i, j = x, y$) are deviatoric stress and

97 strain-rate tensors, respectively; g is the gravitational acceleration; ρ is density. In the heat conservation

98 equation, q_x and q_y are the horizontal and vertical components of the heat flux, respectively; C_p is heat

99 capacity, and H_r, H_a, H_s, and H_L denote the radioactive, adiabatic, shear, and latent heat production,

100 respectively; k is the thermal conductivity.

101 The rheological constitutive relationship connects the deviatoric stress and strain rate:

$$\sigma'_{xx} = 2\eta_{eff}\dot{\varepsilon}_{xx}, \quad \dot{\varepsilon}_{xx} = \frac{\partial v_x}{\partial x}$$

102
$$\sigma'_{xy} = 2\eta_{eff}\dot{\varepsilon}_{xy}, \quad \dot{\varepsilon}_{xy} = \frac{1}{2}\left(\frac{\partial v_x}{\partial y} + \frac{\partial v_y}{\partial x}\right),$$
(4)

$$\sigma'_{yy} = 2\eta_{eff}\dot{\varepsilon}_{yy}, \quad \dot{\varepsilon}_{yy} = \frac{\partial v_y}{\partial y}$$

103   where η_{eff} is the effective viscosity.

2.1.2. Rheology

105   Here we make the conventional assumption that the crust and mantle have a visco-plastic rheology.

106   Viscous deformation is determined as a combination of diffusion and dislocation creep that depends on

107   temperature, pressure, and strain rate, expressed as (Gerya, 2019):

108
$$\eta_{disl} = \frac{1}{2}\frac{1}{(A_D)^{-1/n}(\dot{\varepsilon}_{II})^{(n-1)/n}}\exp\left(\frac{E_a + V_a P}{nRT}\right) * S$$
$$\eta_{diff} = \frac{1}{2}\frac{A_D}{\sigma_{cr}^{(n-1)}}\exp\left(\frac{E_a + V_a P}{RT}\right) * S$$
(5)

109   For mineral aggregates, both dislocation and diffusion creep occur simultaneously, with a combined

110   effective viscosity given by:

111
$$\frac{1}{\eta_{ductile}} = \frac{1}{\eta_{disl}} + \frac{1}{\eta_{diff}},$$
(6)

112   where η_{disl} and η_{diff} are viscosities for dislocation and diffusion creep, respectively. σ_{cr} is the

113   critical stress for the dislocation to diffusion stress transition, and the parameters A_D, E_a, V_a, and n are a

114   material constant, activation energy, activation volume, and stress exponent, respectively, and R is the

115   universal gas constant. The strength scaling factor, S, is introduced as a simple parameter to vary the

116   lithospheric viscosity.

117   Plasticity is implemented using a conventional pseudo-viscous yield criterion first used to study rifting

118   (e.g. Chen and Morgan, 1990) that is extended to include a strain-weakening-like parameterization of

119   fracture-related strain weakening (Gerya et al., 2010; Vogt et al., 2017):

$$\eta_{plastic} = \frac{\sigma_{yield}}{2\dot{\varepsilon}_{\text{II}}}$$

$$\sigma_{yield} = C + P\phi$$

120

$$C = \begin{cases} C_a + (C_b - C_a) \times \dfrac{\gamma}{\gamma_{cr}}, & \text{if } \gamma \leq \gamma_{cr} \\ C_b, & \text{if } \gamma \geq \gamma_{cr} \end{cases},$$ (7)

$$\phi = \begin{cases} \phi_a + (\phi_b - \phi_a) \times \dfrac{\gamma}{\gamma_{cr}}, & \text{if } \gamma \leq \gamma_{cr} \\ \phi_b, & \text{if } \gamma \geq \gamma_{cr} \end{cases}$$

121   where σ_{yield} is yield stress, P is dynamic pressure, γ is the integrated plastic strain, and γ_{cr} is the

122   upper strain limit for fracture-related weakening. C and ϕ are cohesion and friction angle that depend

123   on the plastic value. C_a and ϕ_a are the initial and C_b and ϕ_b are final strength values, respectively.

124   This involves making the rheological assumption that deeply percolating fluids and high pore fluid

125   pressures can significantly lower the plastic strength of fractured rocks.

126   The final effective viscosity is determined by the minimum value between the ductile and plastic

127   viscosities (Ranalli, 1995):

128   $$\eta_{eff} = \min\left(\eta_{ductile}, \eta_{plastic}\right).$$ (8)

129   **2.1.3. Surface processes**

130   Topography in our models evolves according to a transport equation that is solved at each time step,

131   with a crude local parameterization of effects of accounts for sedimentation and erosion:

132   $$\frac{\partial y_{es}}{\partial t} = v_y - v_x \frac{\partial y_{es}}{\partial x} - v_s + v_e.$$ (9)

133   Where y_{es} is the vertical position of the surface as a function of horizontal distance x; and v_x and v_y are

134   the corresponding velocity components, respectively. v_s and v_e are the sedimentation and erosion rates,

135   respectively, conforming to the relation:

136   $v_s = 0$ mm/yr, $v_e = 0.3$ mm/yr when $y_{es} > 5$ km;

137   $v_s = 0.3$ mm/yr, $v_e = 0$ mm/yr when $y_{es} < 5$ km.

138   **2.2. Model Setup**

139   The 2-D numerical model covers a rectangular computational domain of 3000 km $\times$ 700 km and

consists of 1360 × 400 non-uniform grid cells with dozens of mobile markers in each grid cell to transport physical properties (Figure 2a). Above 300 km, the cell-size of the grid in the middle of model (X = 1300 – 2200 km) is 1 km × 1 km, and gradually widens towards the two sides to finally become 5 km × 1 km. From the 300 km depth to the model bottom, each grid is stretched to 5 km in the vertical direction. As a result, the grid in the middle of the model (X = 1300 – 2200 km) is 1 km × 5 km and is 5 km × 5 km in the other regions. Changing resolutions in different model regions can ensure the model can finely depict lithosphere deformation in the region of interest while improving the calculation's efficiency.

In the initial configuration, the model comprises three continental terranes — the Pro-, Mid- and Retro-terrane — which refer to the indenting 'Pro-' terrane driven by plate convergence, an intermediate 'Mid-' terrane, and a far-end backwall 'Retro-' terrane, respectively (Figure 2a). For the purpose of simplification, The the three terranes are assumed to have the same initial crustal structure with 20 km thick upper and lower crust, respectively. In the meanwhile, to simulate lateral structure differences within continental lithosphere (Pasyanos et al., 2014), Thicknesses thicknesses of the initial lithospheric mantle of the Pro-, Mid- and Retro-terrane are 160 km, 90 km, and 120 km, respectively. Variable lithosphere thicknesses for the Pro-, Mid- and Retro-terranes simulate lateral structure differences within continental lithosphere (Pasyanos et al., 2014). The rest of the region is filled by asthenosphere except along the model top, where a 20 km thick layer of "sticky air" with low viscosity (1×10^{18} Pas) and low density (1 kg/m^3) is placed to simulate the effects of a free surface (Schmeling et al., 2008). Flow laws and material properties for each lithospheric layer are listed in Table 1.

Mechanical boundary conditions of the model are that the top and sides are free-slip boundaries which mean that the vertical velocity at the top boundary and horizontal velocity at the side boundaries are all zero., and tThe bottom is assumed to be a somewhat non-physical 'permeable boundary' that was developed to reduce the required depth of the computational region (Burg and Gerya, 2005). For top-driven flows like those considered here, this approximation has been shown to not affect deformation in the upper parts of the region (Burg and Gerya, 2005). Finally, a constant convergence rate of 20 mm/yr is assigned to the Pro-terrane (X = 1000 km) to drive the model.

Initial temperature conditions are set as follows: the model top is set to at 0 °C, the two side boundaries are adiabatic boundaries with zero horizontal heat fluxes, and the model bottom has an initial temperature of 1593 °C, and can dynamically adjust as the model evolves. The initial thermal gradient

in the crust is 15 ℃/km in the three terranes, so their Moho temperature is 600 ℃. A temperature of 1330 ℃ is applied at the bottom of the lithospheric mantle of the three terranes, which leads to the Pro- and Mid-terrane having minimum and maximal thermal gradients in the lithospheric mantle, respectively (see the right plane in Figure 2a). An adiabatic thermal gradient of 0.5 ℃/km is assumed within the asthenosphere. The temperature field would evolve over time, thus, although the three terranes are not in thermal equilibrium at the start of the experiments, it has few effects on model evolution. The initial setup of lithosphere structure and temperature field make the Mid-terrane weakest when same rheology model is used for the three terranes. Finally, a constant convergence rate of 20 mm/yr is assigned to the Pro-terrane (X = 1000 km) to drive the model.

3. Simulation Results

The rheological models of CB-I, CB-II, JS-I, and JS-II assumeresult from different strength scaling factors for the upper crust, the lower crust, and the lithospheric mantle in our numerical models (Figure 2b). We systematically test the effects of these rheological assumptions on the deformation of the Pro-, Mid- and Retro-terranes. According to different behaviors of lithosphere deformation, these Simulation simulation results can be categorized into four basic modes of lithosphere deformation: collision, subduction, thickening and delamination, and replacement (Figures S1 and S2). In the deformation mode of collision, the lithospheric mantle of the Mid-terrane is extruded out and the lithospheric mantles of the two bounding terranes meet and collide together. In the deformation mode of subduction, the lithospheric mantle of one of the bounding terranes subducts into the deep mantle below the Mid-terrane while the other one keeps almost undeformed. In the deformation mode of thickening and delamination, one of the bounding terranes is shortened by compression, and delamination may come on the heels of thickening of lithosphere due to gravitational instability in some cases. In the deformation mode of replacement, the bottom of weak and thick lithospheric mantle of the bounding terrane is scraped off by the strong lithospheric mantle of the Mid-terrane, and replaced by the latter. Here, wWe select a typical case for each mode of lithosphere deformation to discuss describe more details of these modes of model evolution.

3.1. Case 1: Lithosphere Collision

Case 1 represents the scenario of lithosphere collision between the Pro- and Retro-terranes (Figure 3).

198 In this model, the assumed rheological models for the Pro-, Mid- and Retro-terrane are JS-I, JS-II, and

199 JS-I, respectively, which means that the Mid-terrane has a significantly weaker lower crust relative to

200 the Pro- and Retro-terranes. The lithospheric mantle of the Mid-terrane is also slightly weaker due to its

201 thinner lithosphere and correspondingly higher initial temperature field. ~~Strength profiles on the right~~

202 ~~top of Fig. 3 show t~~The lithosphere strength profile~~s~~ of the three terranes are shown in Figure 3g.

203 The Mid-terrane is the first to deform when the Pro-terrane begins to collide, absorbing plate

204 convergence in the form of lithosphere thickening (Figures 3a and 3d). The upper crust of the

205 Mid-terrane breaks due to strain weakening, and several reverse faults ~~with opposite dip directions~~ are

206 form~~ed~~ to absorb crustal shortening. The lower crust folds, and strain diffusely distributes within it.

207 Since the Retro-terrane is relatively strong, it prevents crustal deformation from propagating into this

208 terrane, and restricts the bulk of deformation to the Mid-terrane. With continuous advance of the

209 Pro-terrane and resistance of the Retro-terrane, the crust of the Mid-terrane is intensively shortened,

210 leading to more thrusting structures in the upper crust and a "flower-like" structure in the lower crust

211 (Figures 3b and 3e). Thrust structures and crustal deformation also expand toward the Pro- and

212 Retro-terranes at this stage. Topography also grows towards the two bounding terranes (Figure 7a).

213 Ultimately, the weak lithospheric mantle of the Mid-terrane is squeezed out, and the Pro- and

214 Retro-terrane's lithospheric mantles meet and so start to collide beneath the overlying crust of the

215 Mid-terrane (Figures 3c and 3f).

216 ~~Crustal deformation and topographic uplift first occur in the middle terrane, then expand towards the~~

217 ~~bounding terranes. Ultimately, the lithospheric mantles of the bounding terranes begin to collide after~~

218 ~~extruding/removing the lithospheric mantle beneath the middle terrane.~~

219 **3.2. Case 2: Lithosphere Subduction**

220 Case 2 shows lithosphere subduction of the Pro-terrane (Figure 4). In this model, the assumed

221 rheological models for the Pro-, Mid- and Retro-terrane are JS-II, JS-I, and JS-I, respectively. The

222 Mid-terrane has a stronger lower crust ~~and weaker lithospheric mantle than~~ compared with the

223 Pro-terrane~~.~~ but its lithospheric mantle is a little weaker than the Pro-terrane due to higher temperature

224 field resulting from its thinner lithosphere structure (Figure 4g)~~(see the strength profiles on the right top~~

225 ~~of Figure 4)~~. When convergence begins, the weak lower crust of the Pro-terrane is blocked by the

226 stronger lower crust of the Mid-terrane. This induces it to stack in a collisional front to form a

remarkable folding structure (Figures 4a and 4d). The strong lithospheric mantle of the Pro-terrane continues to move forward and underthrusts beneath the Mid-terrane. As the Pro-terrane advances, its crust gradually enters the Mid-terrane, inducing shortening and thickening of the upper crust of the Mid-terrane, while the strong lower crust of the Mid-terrane almost keeps undeformed (Figures 4b and 4e).

Meanwhile, the lithospheric mantle of the Pro-terrane continues to underthrust and scrapesscraping off part of the lithospheric mantle of the Mid-terrane. Eventually, the crust of the Pro-terrane wedges a long distance into the Mid-terrane, and the lithospheric mantle of the Pro-terrane subducts into the deeper mantle (Figures 4d and 4f). In this example, crustal deformation and topography gradually propagate from the Pro-terrane to the Mid-terrane, whereas the Retro-terrane remains nominally 'undeformed' at all times (Figure 7b).

In some experiments, the lithospheric mantle of the Retro-terrane can subduct beneath the Mid-terrane (Figure S1). In this deformation pattern, (1) crustal deformation and topography gradually propagates from one of the bounding terranes into the other bounding terrane through the middle terrane, and (2) the lithospheric mantle of bounding terrane subducts into the deep mantle beneath the middle terrane.

3.3. Case 3: Lithosphere Thickening and Delamination

Case 3 illustrates the thickening and delamination of the lithospheric mantle of the Pro-terrane (Figure 5). In this case, the rheological models for the Pro-, Mid- and Retro-terranes are CB-II, JS-I, and JS-I, respectively (Figure 5j). The Pro-terrane has a more fragile rheologically weaker lower crust and lithospheric mantle, making it relatively easy to deform once the collision has started. The lithospheric mantlee of the Pro-terrane is first shortened and thickened, and the in which leads to crustal starts to form folding foldin two discrete zones (Figures 5a and 5f)ing. The lower part of the thickened lithospheric mantle is denser than its ambient mantle owing to lower temperature, which causes it to drip downwards (Figures 5b–5h). After delamination of the thickened lithosphere, subduction of the Pro-terrane's lithospheric mantle along one of the deformation localization zones absorbs the plate convergence (Figures 5e and 5i)initiation occurs within the lithospheric mantle of the Pro-terrane. Crustal deformation is restricted in the MidPro-terrane until lithosphere delamination, after which crustal strain and topography rapidly spread from the Pro-terrane to the Mid-terrane (Figure. 7c). Like case 2, the Retro-terrane stays essentially undeformed at all times.

256 If the lithosphere of the Pro- or Retro-terrane is extremely weak, for example, its rheology model is

257 CB-II, then lithosphere thickening and delamination may occur. In this deformation pattern, (1) the

258 weak lithosphere of the bounding terrane first thickens by compression and then delaminates due to its

259 density, while (2) crustal deformation rapidly propagates from the thickened bounding terrane into the

260 middle terrane following lithosphere delamination.

261 **3.4. Case 4: Lithosphere Replacement**

262 Case 4 illustrates how the lithospheric mantle of the Pro-terrane can beis replaced by that of a

263 neighboring stronger Mid-terrane (Figure 6). In this case, the rheological models for the Pro-, Mid- and

264 Retro-terranes are CB-I, JS-II, and JS-I, respectively. The Pro-terrane has a strong lower crust and a

265 thick and weak lithospheric mantle, while the Mid-terrane has a weaker lower crust and a strong

266 lithospheric mantle (Figure 6g). This lithosphere configuration between the Pro- and the Mid-terrane

267 causes deformation to be primarily distributed in the Pro-terrane's lithospheric mantle and the

268 Mid-terrane's crust. As a result, the Mid-terrane's crust becomes intensely shortened by fold and thrust

269 structures, but its strong lithospheric mantle wedges into the Pro-terrane's thick and weak lithospheric

270 mantle (Figures 6a, 6b, 6d and 6e). The strong lithospheric mantle of the Mid-terrane scrapes off the

271 lower part of the weak lithospheric mantle of the Pro-terrane and so replaces it (Figures 6c and 6f).

272 Similar to case 1, crustal deformation and topography expand from the Mid-terrane towards its side

273 terranes (Figure 7d).

274 The lithospheric mantle of the Retro-terrane can also be replaced in some cases (e.g. Figure S1). In this

275 deformation pattern, the significant deformation features are that: (1) part of the weak lithospheric

276 mantle of the bounding terrane is replaced by the strong lithospheric mantle of the middle terrane; (2)

277 crustal deformation and topography expand from center towards the two sides.

278 **4. Discussion**

279 **4.1. Rheological Characteristics for Distinct Lithosphere Deformation Patterns**

280 Distinct lithosphere deformation patterns in our simulations results result arise from rheological

281 contrasts between neighboring continental terranes. Figure 8 summarizes the rheological characteristics

282 of these distinct deformation patterns (Figure 8). When the Mid-terrane's lithospheric mantle is

283 weakest (typified by models in which the rheological model of the Mid-terrane is CB-II), it is easy for

its mantle to be extruded out, leading to collision between the lithospheric mantles of its surrounding Pro- and Retro-terranes. When one of the two bounding Pro- or Retro-terrane's has extremely weak lithospheric mantle is weakest, its lithosphere is first to be thickened by compression, and then delaminatedion may follow due to the resulting density-driven instability. When the lower crust of the Mid-terrane is relatively strong (CB-I or JS-I), while the lower crustit is weaker in the Pro- or Retro-terrane (CB-II or JS-II), then the lithospheric mantle of the Pro- or Retro-terrane will tend to subduct into the deep mantle, e.g. leading to intracontinental subduction. Finally, when the Mid-terrane has a weak lower crust and strong lithospheric mantle (JS-II), while the Pro- or Retro-terrane has a strong lower crust and weak lithospheric mantle (CB-I), then the lithospheric mantle of the former may replaces the lithospheric mantle of the latter.

In When the deformation patterns involve the collision and replacement of lithosphere, continental deformation involves all three terranes (Figures 3 and 6). In contrast, the other deformation patterns only involve two terranes, the Pro- or Retro-terrane and the Mid-terrane (Figures 4 and 5). The rheological properties of the Mid-terrane are responsible for these differences. Like previous numerical studies (Kelly et al., 2016, 2020; Li et al., 2016; Huangfu et al., 2018, 2022; Sun and Liu, 2018), our simulations show that a weak a Mid-terrane is easier to deform, and that in this case lithosphere deformation will expand from center to its neighboring sides; while a relatively strong Mid-terrane prevents deformation from propagating far, so that lithosphere deformation is constrained to occur within two terranes. The simulation results also highlight the potential effects of differences in rheological stratification between different terranes to lithosphere deformation (Figures 4 and 6).

Although our multi-terrane numerical models mainly focus on the impact of the lateral strength differences between different terranes in a continental collisional system, rheological models of CB-I, CB-II, JS-I, JS-II also involve vertical rheological variation (Figure 1a). It seems difficult to summarize how vertical strength variation affects lithosphere deformation of the continental collisional system. For example, in some cases, only changing the rheological models of the Pro- or Retro-terranes may produce distinct deformation modes such as collision, subduction, thickening and delamination, and displacement (e.g., the first and third rows, the third column in the upper left panel in Figure 8 and the third column in the lower right panel in Figure 8). However, changing the rheological models of the Pro- or Retro-terranes seems to have less impact on the deformation mode of the continental collisional system, according to the simulation results of models which are connected by several cross-shaped

solid lines with different colors in Figure 8. Thus, it is difficult to determine whether the horizontal strength contrasts between terranes or the vertical strength variation of a single terrane plays the dominant role in a multi-terrane collisional system. This is also the significance and necessity of our study.

4.2. Influences of Lithosphere Structure

Lithospheric thickness is one of the critical factors that controls its strength (Burov, 2011);), this and it can strongly vary between tectonic regions (Pasyanos et al., 2014). In our models, we assume different lithospheric thicknesses for the Pro-, Mid- and Retro-terrane to explore these effects. Complex effects are seen. When changing the lithospheric thicknesses of the Mid-terrane, or of all three terranes, remarkable variations in lithosphere deformation appear in cases 1 and 2, but smaller variations are seen for cases 3 and 4 (Figure 9). Cases 1 and 2 assume a Jelly sandwich rheology for the Pro-, Mid- and Retro-terrane, so the strength of the lithospheric mantle of three terranes is comparable. Strength variations produced by differences in lithospheric thickness may alter the relative strength of the three terranes, resulting in distinct lithospheric deformations. For example, if the Pro- and Mid-terranes have same lithosphere thickness, deformation mode in Case 2 would change from subduction to thickening (subplot 3 vs. subplot 8 in Figure 9); if the Mid-terrane is thickest or the three terranes have same thickness of lithosphere, deformation mode in Case 1 would change from collision to replacement (subplot 2 vs. subplot 17 and 22 in Figure 9), and the polarity of the subduction of Pro-terrane's lithospheric mantle would be reversed in Case 2 (subplot 3 vs. subplot 18 and 23 in Figure 9). Instead, in cases 3 and 4, the Pro-, Mid- and Retro-terrane have two regions with stronger Jelly-sandwich-like rheological structures and one with a weaker Crème brûlée structure, and deformation preferentially concentrates in the weaker terrane with ta weak mantle Crème brûlée rheology. In comparison to the large strength difference implied for the lithospheric mantle between the Crème brûlée and Jelly Sandwich rheological models, the strength variations associated with the differences in lithosphere thickness are relatively small. Therefore, changing the thicknesses of the lithosphere has much smaller effects on the lithosphere deformation, as seen in cases 3 and 4 (also see the subplots in 3rd and 4rd rows of Figure 9).

In addition, the weak zones that suture two terranes are generally preserved during continental amalgamation (Burker et al., 1977; Vink et al., 1984; Yin and Harrison, 2000). These local pre-existing

lithosphere weaknesses would be preferentially activated if the continental lithosphere were subjected to compression, and could play a key role in concentrating deformation, adjusting deformation sequences, and inducing lithosphere subduction (Sokoutis and Willingshofer, 2011; Heron et al., 2016; Chen et al., 2020; Xie et al., 2021, 2023). Comparing the simulation results of models with and without weak zone, we find that a weak zone will facilitate lithosphere subduction in earlier stages of model evolution, resulting in more diverse lithosphere deformation patterns during the later stage (Figure S210).

4.3. Implications for the Tectonics of East Asia Eurasia

4.3.1. Lithosphere Collision beneath the Eastern Tien Shan

The eastern Tien Shan is an ideal region to study the deformation patterns linked to long-term lithosphere collision (Figure 11a). The eastern Tien Shan is located east of the geographic longitude of 80° E and is bounded by the Tarim Basin to the south, and the Junggar Basin to the north (Figure 10a). It is composed of a series of former island arcs and small continental blocks that amalgamated during the late Paleozoic (Han and Zhao, 2017). The lithosphere of the eastern Tien Shan is weaker and thinner in comparison to its neighboring Tarim Basin and Junggar Basin (Kumar et al., 2005; Lei and Zhao et al., 2007; Zhang et al., 2013; Deng and Tesauro, 2016). At ~20 – 25 Ma, the eastern Tien Shan became a reactivated orogeny in response to ongoing India-Asia collision (Yin et al., 1998). Compression linked to the India-Asia collision induced the Tarim lithosphere to underthrust northward (Xu et al., 2002; Guo et al., 2006; Lei and Zhao et al., 2007; Lü et al., 2019; Hapaer et al., 2022; Sun et al., 2022). In the northern part of the eastern Tien Shan, significant high-velocity anomalies and Moho overlap are also imaged, which are conventionally explained as being due to the southward underthrusting of the Junggar lithosphere (Xu et al., 2002; Guo et al., 2006; Li et al., 2016; Lü et al., 2019). High-velocity anomalies in the Tarim and Junggar lithosphere appear to connect beneath the eastern Tien Shan, suggesting the lithosphere of the Tarim and Junggar Basins has converged and collided together in this region (Figure 10b 11band 11c; Lü et al., 2019). Bidirectional underthrusting of the Tarim and Junggar lithosphere leads to intense crustal shortening and thrust faults on both flanks over the adjacent basins, as well as attendant fold and reverse fault zones along the range fronts (Yin et al., 1998; Wang et al., 2004).

4.3.2. Lithosphere Thickening and Delamination in the Tibetan Plateau

The deformation pattern arising from lithosphere thickening and delamination has been applied to the Tibetan Plateau (Figure 11c). Tibetan lithosphere may have been significantly weakened by hydration, metasomatism, and partial melting of the lithospheric mantle during a series of oceanic closure and terrane accretion events before the India-Asia collision (Yin and Harrison, 2000; Zhang et al., 2014; Ma et al., 2021). It was then pushed northward by the Indian craton and was blocked by the Tarim/Qaidam craton during India-Asia collision, leading to double crustal thickness (Zhao and Morgan, 1985; Zhang et al., 2011). The lithosphere beneath the Tibetan Plateau does not thicken significantly like its crust, especially beneath northern Tibet (Owens and Zandt, 1997; Tunini et al., 2016). Numerous observations instead suggest that the Tibetan lithosphere has been detached from the crust and has sunk into deeper mantle, consistent with the presence of high-velocity regions in the deep mantle in western, southern and southeastern Tibet (Li et al., 2008; Chen et al., 2017; Feng et al., 2021). A significant depression of the 660-km discontinuity beneath the Himalaya terrane and the uplift of 410-km discontinuity in western Tibet have also attributed to the presence of delaminated Tibetan lithosphere (Wu et al., 2022). In northern Tibet, anomalously high temperatures are assumed to be linked to a region of inefficient S_n propagation indicating a thin or absent lithospheric mantle lid in this region, while a remarkable low-velocity zone in the mantle and ultra-potassic volcanics also suggest lithosphere thinning (Barazangi and Ni, 1982; Turner et al., 1996; Owens and Zandt, 1997; Guo et al., 2006; Liang et al., 2012; Tunini et al., 2016). After lithosphere thinning commenced in the Miocene, the Tibetan Plateau rapidly grew outwards rapidly (Lu et al., 2018 and references therein; Molnar et al., 1993; Xie et al., 2023).

4.3.3. Lithosphere Subduction in Southeastern China

An example of intracontinental subduction is the Early Paleozoic Orogen in Southeastern China which appears to have not been preceded by oceanic subduction (Figure 11d; Faure et al., 2009). The Early Paleozoic Orogen of Southeastern China is located on the Wuyi-Yunkai Fold Belt. Arguments against it being a collisional orogenic belt are its lack of preserved ophiolites, a magmatic arc, subduction complexes, and high-pressure metamorphism. Instead, structural, metamorphic, and sedimentary elements indicate that this orogen was an intracontinental orogen controlled by the northward subduction of Cathaysia (Faure et al., 2009). A weak suture/failure zone inherited from previous

tectonic events contributed to the internal subduction of Cathaysia, during which ductile decollements accommodated horizontal shortening by folding and thrusting. The tectonic development of this orogen appears similar to the deformation mode of lithosphere subduction (Figure 4).

So far, we have yet to find a suitable region to apply the model deformation pattern of lithosphere replacement. In this deformation pattern, crustal deformation and topographic evolution are similar to those in the deformation pattern of lithosphere collision (Figures 7a and 7c). Thus, it is not easy to identify this pattern by geological and geophysical techniques when the replaced and original continental lithosphere has similar properties. Improved imaging observations with better resolution may allow this deformation pattern to be identified in the future.

5. Model Limitations

Although we can obtain four deformation modes of continental lithosphere by changing the rheologies of different terranes in a collisional model, we must keep in mind that our results are based on some simplifications and assumptions, which may affect the model results. For example, in our model three terranes are directly collaged together, but in nature different terranes are often connected through weak sutures which may preferentially deform when they are subjected to compression (Burker et al., 1977; Yin and Harrison, 2000). These local pre-existing weak zones have non-negligible influences on lithospheric deformation, and their role were widely discussed in previous studies (Sokoutis and Willingshofer, 2011; Heron et al., 2016; Chen et al., 2020 ; Xie et al., 2021, 2023). We also discussed the effects of local pre-existing weak zones in Section 4.2. In addition, lithosphere thicknesses of the Pro-, Mid- and Retro-terranes are chose arbitrary in our models, but they also has important influences on lithosphere deformation (Figure 9). Some studies believe that differences in crustal strength will also cause different lithospheric deformation (Faccenda et al., 2008; Vogt et al., 2017, 2018), but the three terranes are set same crustal structure in our model for the aim of simplification. As well, some studies believe that the convergence rate will greatly affect the deformation of orogenic belts (Chen et al., 2016; Vogt et al., 2017), but in this study, the impact of the convergence rate almost can be ignored.

65. Conclusions

The continental lithosphere is likely to have strong lateral variations in its strength. We explored 2-D

numerical models that contain three diverse types of continental terranes to study the responses of continental terranes with different strengths to compression. Four rheological models were respectively applied to each of the Pro-, Mid- and Retro-terranes, and simulation results can be grouped into four distinct deformation styles: lithosphere collision, subduction, thickening and delamination, and replacement. These deformation styles arise from the rheological contrasts between these terranes: (1) when the middle terrane is the weakest, its lithosphere is easily extruded, which leads to lithosphere collision between its two bounding terranes; (2) when the middle terrane has a strong lower crust, while the lower crust of a bounding terrane is weak, then subduction of the lithosphere of the bounding terrane will occur; (3) when a bounding terrane is the weakest, its lithosphere would tend to be thickened by lateral compression, followed by lithosphere delamination due to the resulting density/gravitational instability; (4) when a bounding terrane has a strong lower crust and weak lithospheric mantle, while the middle terrane has a weak lower crust and strong lithospheric mantle, then lithosphere replacement will again occur. These simulation patterns are seen in observed deformation patterns and structures in the eastern Tien Shan, and the Tibetan Plateau, the Early Paleozoic Orogen of Southeastern China, suggesting they are likely to be naturally occurring modes of intracontinental orogenesis.

Code availability

Requests for the numerical code I2VIS should be sent to the main developer (taras.gerya@erdw.ethz.ch).

Data availability

Numerical modeling data and the model evolution animations of Cases 1 – 4 are all provided in Zenodo (https://doi.org/10.5281/zenodo.8354366 and https://doi.org/10.5281/zenodo.10731981).

Author contribution: **Conceptualization:** Yongshun John Chen; **Methodology:** Lin Chen, Renxian Xie; **Investigation:** Renxian Xie; **Formal analysis:** Renxian Xie, Lin Chen; **Visualization:** Renxian Xie, Jason P. Morgan; **Writing – original draft preparation:** Renxian Xie; **Funding acquisition:** Yongshun John Chen, Lin Chen, Renxian Xie.

Competing interests: The authors declare that they have no conflict of interest.

Disclaimer. Publisher's note: Copernicus Publications remains neutral with regard to jurisdictional claims in published maps and institutional affiliations.

Acknowledgments

The authors sincerely thank Prof. Taras Gerya for providing the I2VIS package and his long-lasting guidance on our geodynamic modeling. The authors acknowledge that figures of simulation results were prepared with the Generic Mapping Tools (GMT, http://www.soest.hawaii.edu/gmt/). All models were performed on the TianHe-1A system at the National Supercomputer Center in Tianjin.

Financial support: This study was supported by the National Natural Science Foundation of China (Grants U1901602) and, the National Key R&D Program of China (2022YFF0800800) and National Natural Science Foundation of China (42374076).

References

Artemieva, I. M.: Global 1×1 thermal model TC1 for the continental lithosphere: implications for lithosphere secular evolution, Tectonophysics, 416, 245-277, https://doi.org/10.1016/j.tecto.2005.11.022, 2006.

Audet, P., and Bürgmann, R.: Dominant role of tectonic inheritance in supercontinent cycles, Nature geoscience, 4, 184-187, https://doi.org/10.1038/ngeo1080, 2011.

Barazangi, M., and Ni, J.: Velocities and propagation characteristics of Pn and Sn beneath the Himalayan arc and Tibetan plateau: Possible evidence for underthrusting of Indian continental lithosphere beneath Tibet, Geology, 10, 179-185,

https://doi.org/10.1130/0091-7613(1982)10<179:VAPCOP>2.0.CO;2, 1982.

Burg, J. P., and Gerya, T. V.: The role of viscous heating in Barrovian metamorphism of collisional orogens: thermomechanical models and application to the Lepontine Dome in the Central Alps, Journal of Metamorphic Geology, 23, 75-95, https://doi.org/10.1111/j.1525-1314.2005.00563.x, 2005.

Burke, K., Dewey, J. F., and Kidd, W. S. F.: World distribution of sutures—the sites of former oceans, Tectonophysics, 40, 69-99, https://doi.org/10.1016/0040-1951(77)90030-0, 1977.

Burov, E. B., and Watts, A. B.: The long-term strength of continental lithosphere:" jelly sandwich" or" crème brûlée"?. GSA today, 16, 4. , doi: 10.1130/1052-5173(2006)016<4:tltSOc>2.0.cO;2, 1997, 2006.

Burov, E. B.: Rheology and strength of the lithosphere, Marine and petroleum Geology, 28, 1402-1443, https://doi.org/10.1016/j.marpetgeo.2011.05.008, 2011.

Bürgmann, R., and Dresen, G.: Rheology of the lower crust and upper mantle: Evidence from rock mechanics, geodesy, and field observations, Annu. Rev. Earth Planet. Sci., 36, 531-567, doi: 10.1146/annurev.earth.36.031207.124326, 2008.

Chen, M., Niu, F., Tromp, J., Lenardic, A., Lee, C. T. A., Cao, W., and Ribeiro, J.: Lithospheric foundering and underthrusting imaged beneath Tibet, Nature communications, 8, 15659, https://doi.org/10.1038/ncomms15659, 2017.

Chen, L.: The role of lower crustal rheology in lithospheric delamination during orogeny, Frontiers in Earth Science, 9, 755519, doi: 10.3389/feart.2021.755519, 2021.

Chen, L., Capitanio, F. A., Liu, L., and Gerya, T. V.: Crustal rheology controls on the Tibetan plateau formation during India-Asia convergence, Nature Communications, 8, 15992, https://doi.org/10.1038/ncomms15992, 2017.

Chen, L., & Gerya, T. V.: The role of lateral lithospheric strength heterogeneities in orogenic plateau growth: Insights from 3-D thermo-mechanical modeling, Journal of Geophysical Research: Solid Earth, 121, 3118–3138, https://doi.org/10.1002/2016JB012872.

Chen, L., Liu, L., Capitanio, F. A., Gerya, T. V., and Li, Y.: The role of pre-existing weak zones in the formation of the Himalaya and Tibetan plateau: 3-D thermomechanical modelling, Geophysical Journal International, 221, 1971-1983, doi: 10.1093/gji/ggaa125, 2020.

Chen, W. P., and Molnar, P.: Focal depths of intracontinental and intraplate earthquakes and their

503   implications for the thermal and mechanical properties of the lithosphere, Journal of Geophysical

504   Research: Solid Earth, 88, 4183-4214, https://doi.org/10.1029/JB088iB05p04183, 1983.

505   Chen Y, Morgan W J.: Rift valley/no rift valley transition at mid-ocean ridges, Journal of Geophysical

506   Research: Solid Earth, 95(B11): 17571-17581, https://doi.org/10.1029/JB095iB11p17571, 1990.

507   Cook, K. L., and Royden, L. H.: The role of crustal strength variations in shaping orogenic plateaus,

508   with application to Tibet, Journal of Geophysical Research: Solid Earth, 113,

509   https://doi.org/10.1029/2007JB005457, 2008.

510   Deng, Y., and Tesauro, M.: Lithospheric strength variations in Mainland China: Tectonic implications.

511   Tectonics, 35, 2313–2333, https://doi.org/10.1002/2016TC004272, 2016.

512   Faccenda, M., Gerya, T. V., and Chakraborty, S.: Styles of post-subduction collisional orogeny:

513   Influence of convergence velocity, crustal rheology and radiogenic heat production, Lithos, 103,

514   257-287, https://doi.org/10.1016/j.lithos.2007.09.009, 2008.

515   Faure, M., Shu, L., Wang, B., Charvet, J., Choulet, F., and Monie, P.: Intracontinental subduction: a

516   possible mechanism for the Early Palaeozoic Orogen of SE China, Terra Nova, 21, 360-368,

517   https://doi.org/10.1111/j.1365-3121.2009.00888.x, 2009.

518   Feng, J., Yao, H., Chen, L., and Wang, W.: Massive lithospheric delamination in southeastern Tibet

519   facilitating continental extrusion, National Science Review, 9, nwab174, DOI:

520   10.1093/nsr/nwab174, 2022.

521   Gerya, T.: Dynamical instability produces transform faults at mid-ocean ridges, Science, 329,

522   1047-1050, DOI: 10.1126/science.1191349, 2010.

523   Gerya, T.: Introduction to numerical geodynamic modelling, 2nd edition, Cambridge University Press,

524   488pp, ISBN: 9781316534243, https://doi.org/10.1017/9781316534243, 2019.

525   Gerya, T. V., and Yuen, D. A.: Characteristics-based marker-in-cell method with conservative

526   finite-differences schemes for modeling geological flows with strongly variable transport

527   properties, Physics of the Earth and Planetary Interiors, 140, 293-318,

528   https://doi.org/10.1016/j.pepi.2003.09.006, 2003.

529   Guo, B., LIU, Q. Y., CHEN, J. H., ZHAO, D. P., LI, S. C., and LAI, Y. G.: Seismic tomography of the

530   crust and upper mantle structure underneath the Chinese Tianshan, Chinese Journal of Geophysics,

531   49, 1543-1551, https://doi.org/10.1002/cjg2.982, 2006.

532   Hacker, B. R., Kelemen, P. B., and Behn, M. D.: Continental lower crust, Annual Review of Earth and

533   Planetary Sciences, 43, 167-205, doi: 10.1146/annurev-earth-050212-124117, 2015.

534   Han, Y., and Zhao, G.: Final amalgamation of the Tianshan and Junggar orogenic collage in the

535   southwestern Central Asian Orogenic Belt: Constraints on the closure of the Paleo-Asian Ocean,

536   Earth-Science Reviews, 186, 129-152, https://doi.org/10.1016/j.earscirev.2017.09.012, 2018.

537   Hapaer, T., Tang, Q., Sun, W., Ao, S., Zhao, L., Hu, J., ... and Xiao, W.: Opposite facing dipping

538   structure in the uppermost mantle beneath the central Tien Shan from Pn traveltime tomography,

539   International Journal of Earth Sciences, 111, 2571-2584,

540   https://doi.org/10.1007/s00531-022-02162-9, 2022.

541   Heron, P. J., and Pysklywec, R. N.: Inherited structure and coupled crust-mantle lithosphere evolution:

542   Numerical models of Central Australia, Geophysical Research Letters, 43, 4962-4970,

543   https://doi.org/10.1002/2016GL068562, 2016.

544   Heron, P. J., Pysklywec, R. N., and Stephenson, R.: Lasting mantle scars lead to perennial plate

545   tectonics, Nature communications, 7, 11834, https://doi.org/10.1038/ncomms11834, 2016.

546   Huangfu, P., Li, Z. H., Gerya, T., Fan, W., Zhang, K. J., Zhang, H., and Shi, Y.: Multi-terrane structure

547   controls the contrasting lithospheric evolution beneath the western and central–eastern Tibetan

548   plateau, Nature Communications, 9, 3780, https://doi.org/10.1038/s41467-018-06233-x, 2018.

549   Huangfu, P., Li, Z. H., Fan, W., Zhang, K. J., and Shi, Y.: Contrasting collision-induced far-field

550   orogenesis controlled by thermo-rheological properties of the composite terrane, Gondwana

551   Research, 103, 404-423, https://doi.org/10.1016/j.gr.2021.10.020, 2022.

552   Jackson, J. A.: Strength of the continental lithosphere: time to abandon the jelly sandwich?, GSA today,

553   12, 4-10, DOI: 10.1130/1052-5173(2002)012<0004:SOTCLT>2.0.CO;2, 2002.

554   Junmeng, Z., Guodong, L., Zaoxun, L., Xiankang, Z., and Guoze, Z.: Lithospheric structure and

555   dynamic processes of the Tianshan orogenic belt and the Junggar basin, Tectonophysics, 376,

556   199-239, https://doi.org/10.1016/j.tecto.2003.07.001, 2003.

557   Kelly, S., Butler, J. P., and Beaumont, C.: Continental collision with a sandwiched accreted terrane:

558   Insights into Himalayan–Tibetan lithospheric mantle tectonics?, Earth and Planetary Science

559   Letters, 455, 176-195, https://doi.org/10.1016/j.epsl.2016.08.039, 2016.

560   Kelly, S., Beaumont, C., and Butler, J. P.: Inherited terrane properties explain enigmatic post-collisional

561   Himalayan-Tibetan evolution, Geology, 48, 8-14, https://doi.org/10.1130/G46701.1, 2020.

562   Kumar, P., Yuan, X., Kind, R., and Kosarev, G.: The lithosphere-asthenosphere boundary in the Tien

563   Shan-Karakoram region from S receiver functions: Evidence for continental subduction,

564   Geophysical Research Letters, 32, https://doi.org/10.1029/2004GL022291, 2005.

565 Lei, J., and Zhao, D.: Teleseismic P-wave tomography and the upper mantle structure of the central

566   Tien Shan orogenic belt, Physics of the Earth and Planetary Interiors, 162, 165-185,

567   https://doi.org/10.1016/j.pepi.2007.04.010, 2007.

568 Li, C., Van der Hilst, R. D., Meltzer, A. S., and Engdahl, E. R.: Subduction of the Indian lithosphere

569   beneath the Tibetan Plateau and Burma, Earth and Planetary Science Letters, 274, 157-168,

570   https://doi.org/10.1016/j.epsl.2008.07.016, 2008.

571 Li, J., Zhang, J., Zhao, X., Jiang, M., Li, Y., Zhu, Z., ... and Yang, T.: Mantle subduction and uplift of

572   intracontinental mountains: A case study from the Chinese Tianshan Mountains within Eurasia,

573   Scientific Reports, 6, 28831, https://doi.org/10.1038/srep28831, 2016.

574 Li, Z. H., Liu, M., and Gerya, T.: Lithosphere delamination in continental collisional orogens: A

575   systematic numerical study, Journal of Geophysical Research: Solid Earth, 121, 5186-5211,

576   https://doi.org/10.1002/2016JB013106, 2016.

577 Liang, X., Sandvol, E., Chen, Y. J., Hearn, T., Ni, J., Klemperer, S., ... & Tilmann, F.: A complex

578   Tibetan upper mantle: A fragmented Indian slab and no south-verging subduction of Eurasian

579   lithosphere, Earth and Planetary Science Letters, 333, 101-111,

580   https://doi.org/10.1016/j.epsl.2012.03.036, 2012.

581 Lu, H., Tian, X., Yun, K., and Li, H.: Convective removal of the Tibetan Plateau mantle lithosphere by~

582   26 Ma, Tectonophysics, 731, 17-34, https://doi.org/10.1016/j.tecto.2018.03.006, 2018.

583 Lü, Z., Gao, H., Lei, J., Yang, X., Rathnayaka, S., and Li, C.: Crustal and upper mantle structure of the

584   Tien Shan orogenic belt from full-wave ambient noise tomography, Journal of Geophysical

585   Research: Solid Earth, 124, 3987-4000, https://doi.org/10.1029/2019JB017387, 2019.

586 Ma, L., Wang, Q., Kerr, A. C., and Tang, G. J.: Nature of the pre-collisional lithospheric mantle in

587   central Tibet: Insights to Tibetan Plateau uplift, Lithos, 388, 106076,

588   https://doi.org/10.1016/j.lithos.2021.106076, 2021.

589 Mitchell, R. N., Zhang, N., Salminen, J., Liu, Y., Spencer, C. J., Steinberger, B., ... and Li, Z. X. : The

590   supercontinent cycle, Nature Reviews Earth and Environment, 2, 358-374,

591   https://doi.org/10.1038/s43017-021-00160-0, 2021.

592 Molnar, P., England, P., and Martinod, J.: Mantle dynamics, uplift of the Tibetan Plateau, and the Indian

monsoon, Reviews of Geophysics, 31, 357-396, https://doi.org/10.1029/93RG02030, 1993.

Morgan J P, Vannucchi P. : Transmogrification of ocean into continent: implications for continental evolution, Proceedings of the National Academy of Sciences, 119(15): e2122694119, https://doi.org/10.1073/pnas.2122694119, 2022.Owens, T. J., and Zandt, G.: Implications of crustal property variations for models of Tibetan plateau evolution, Nature, 387, 37-43, https://doi.org/10.1038/387037a0, 1997.

Pasyanos, M. E., Masters, T. G., Laske, G., and Ma, Z.: LITHO1. 0: An updated crust and lithospheric model of the Earth, Journal of Geophysical Research: Solid Earth, 119, 2153-2173, https://doi.org/10.1002/2013JB010626, 2014.

Ranalli, G.: Rheology of the Earth, 2nd Edition, Springer Science and Business Media, 421pp, ISBN 0412546701, 1995.

Schmeling, H., Babeyko, A. Y., Enns, A., Faccenna, C., Funiciello, F., Gerya, T., ... and Van Hunen, J.: A benchmark comparison of spontaneous subduction models—Towards a free surface, Physics of the Earth and Planetary Interiors, 171, 198-223, https://doi.org/10.1016/j.pepi.2008.06.028, 2008.

Sokoutis, D., and Willingshofer, E.: Decoupling during continental collision and intra-plate deformation, Earth and Planetary Science Letters, 305, 435-444, https://doi.org/10.1016/j.epsl.2011.03.028, 2011.

Sun, W., Ao, S., Tang, Q., Malusà, M. G., Zhao, L., and Xiao, W.: Forced Cenozoic continental subduction of Tarim craton-like lithosphere below the Tianshan revealed by ambient noise tomography, Geology, 50, 1393-1397, https://doi.org/10.1130/G50510.1, 2022.

Sun, Y., and Liu, M.: Rheological control of lateral growth of the Tibetan Plateau: Numerical results, Journal of Geophysical Research: Solid Earth, 123, 10-124, https://doi.org/10.1029/2018JB016601, 2018.

Tunini, L., Jimenez-Munt, I., Fernandez, M., Verges, J., Villasenor, A., Melchiorre, M., and Afonso, J. C.: Geophysical-petrological model of the crust and upper mantle in the India-Eurasia collision zone, Tectonics, 35, 1642–1669, https://doi.org/10.1002/2016TC004161, 2016.

Turner, S., Arnaud, N., Liu, J., Rogers, N., Hawkesworth, C., Harris, N., ... and Deng, W.: Post-collision, shoshonitic volcanism on the Tibetan Plateau: implications for convective thinning of the lithosphere and the source of ocean island basalts, Journal of petrology, 37, 45-71, https://doi.org/10.1093/petrology/37.1.45, 1996.

623 Vink G E, Morgan W J, Zhao W L: Preferential rifting of continents: a source of displaced terranes[J].

624 Journal of Geophysical Research: Solid Earth, 89(B12): 10072-10076,

625 https://doi.org/10.1029/JB089iB12p10072, 1984.

626 Vogt, K., Matenco, L., and Cloetingh, S.: Crustal mechanics control the geometry of mountain belts.

627 Insights from numerical modelling, Earth and Planetary Science Letters, 460, 12-21,

628 https://doi.org/10.1016/j.epsl.2016.11.016, 2017.

629 Vogt, K., Willingshofer, E., Matenco, L., Sokoutis, D., Gerya, T., and Cloetingh, S.: The role of lateral

630 strength contrasts in orogenesis: A 2D numerical study, Tectonophysics, 746, 549-561,

631 https://doi.org/10.1016/j.tecto.2017.08.010, 2018.

632 Wang, C. Y., Yang, Z. E., Luo, H., and Mooney, W. D.: Crustal structure of the northern margin of the

633 eastern Tien Shan, China, and its tectonic implications for the 1906 M~7.7 Manas earthquake,

634 Earth and Planetary Science Letters, 223, 187-202, https://doi.org/10.1016/j.epsl.2004.04.015,

635 2004.

636 Wang, M., and Shen, Z. K.: Present-day crustal deformation of continental China derived from GPS

637 and its tectonic implications, Journal of Geophysical Research: Solid Earth, 125, e2019JB018774,

638 https://doi.org/10.1029/2019JB018774, 2020.

639 Wu, Y., Bao, X., Zhang, B., Xu, Y., and Yang, W.: Seismic evidence for stepwise lithospheric

640 delamination beneath the Tibetan Plateau, Geophysical Research Letters, 49, e2022GL098528,

641 https://doi.org/10.1029/2022GL098528, 2022.

642 Xie, R., Chen, L., Xiong, X., Wang, K., and Yan, Z.: The Role of Pre-existing Crustal Weaknesses in

643 the Uplift of the Eastern Tibetan Plateau: 2D Thermo-Mechanical Modeling, Tectonics, 40,

644 e2020TC006444, https://doi.org/10.1029/2020TC006444, 2021.

645 Xie, R., Chen, L., Yin, A., Xiong, X., Chen, Y. J., Guo, Z., and Wang, K.: Two phases of crustal

646 shortening in northeastern Tibet as a result of a stronger Qaidam lithosphere during the Cenozoic

647 India–Asia collision, Tectonics, 42, e2022TC007261, https://doi.org/10.1029/2022TC007261,

648 2023.

649 Xu, Y., Liu, F., Liu, J., and Chen, H.: Crust and upper mantle structure beneath western China from P

650 wave travel time tomography, Journal of Geophysical Research: Solid Earth, 107, ESE-4,

651 https://doi.org/10.1029/2001JB000402, 2002.

652 Yin, A., Nie, S., Craig, P., Harrison, T. M., Ryerson, F. J., Xianglin, Q., and Geng, Y.: Late Cenozoic

653 tectonic evolution of the southern Chinese Tian Shan, Tectonics, 17, 1-27,

654 https://doi.org/10.1029/97TC03140, 1998.

655 Yin, A., and Harrison, T. M.: Geologic evolution of the Himalayan-Tibetan orogen, Annual review of

656 earth and planetary sciences, 28, 211-280, https://doi.org/10.1146/annurev.earth.28.1.211, 2000.

657 Zhang, Z., Deng, Y., Teng, J., Wang, C., Gao, R., Chen, Y., and Fan, W.: An overview of the crustal

658 structure of the Tibetan plateau after 35 years of deep seismic soundings, Journal of Asian Earth

659 Sciences, 40, 977-989, https://doi.org/10.1016/j.jseaes.2010.03.010, 2011.

660 Zhang, Z., Deng, Y., Chen, L., Wu, J., Teng, J., and Panza, G.: Seismic structure and rheology of the

661 crust under mainland China, Gondwana Research, 23, 1455-1483,

662 https://doi.org/10.1016/j.gr.2012.07.010, 2013.

663 Zhang, Z., Teng, J., Romanelli, F., Braitenberg, C., Ding, Z., Zhang, X., ... & Panza, G. F.: Geophysical

664 constraints on the link between cratonization and orogeny: Evidence from the Tibetan Plateau and

665 the North China Craton. Earth-Science Reviews, 130, 1-48,

666 https://doi.org/10.1016/j.earscirev.2013.12.005, 2014.

667 Zhao W L, Morgan W J.: Uplift of Tibetan plateau, Tectonics, 4(4),

668 359-369, https://doi.org/10.1029/TC004i004p00359, 1985.

669

670

Figures and captions
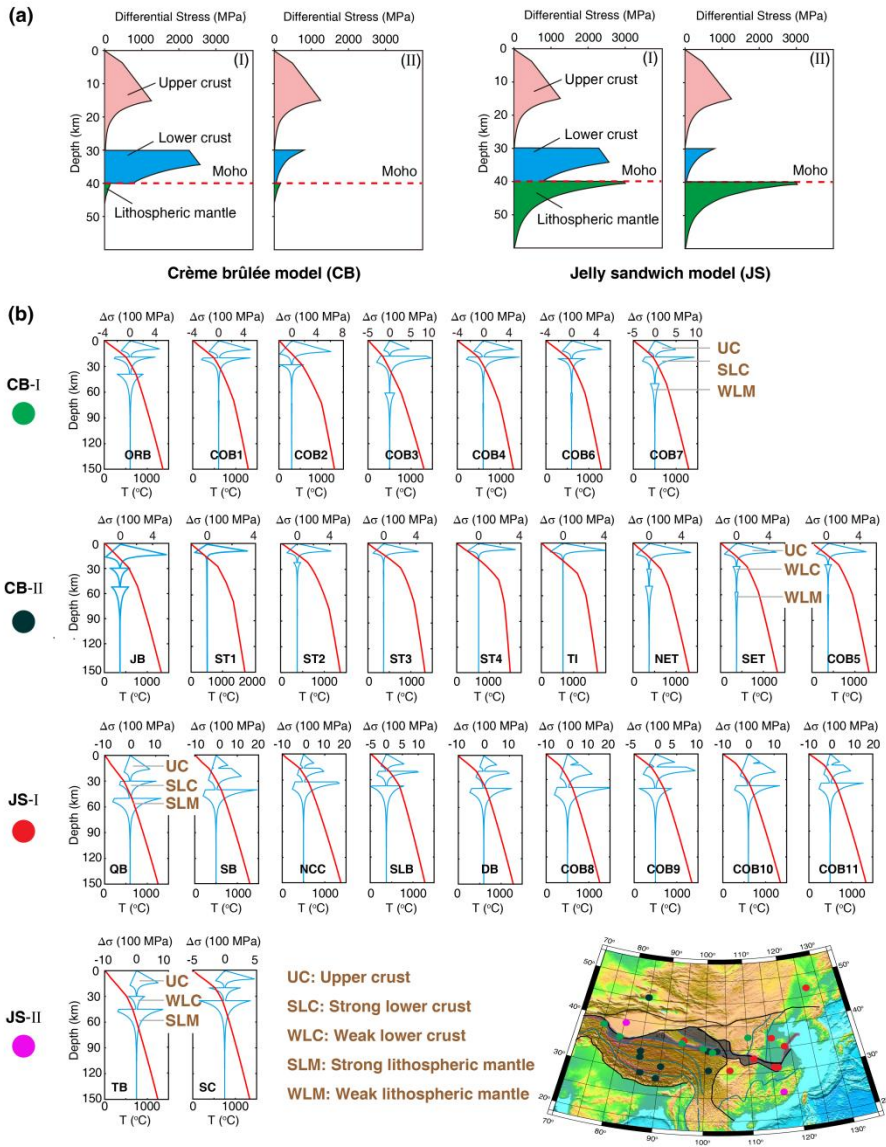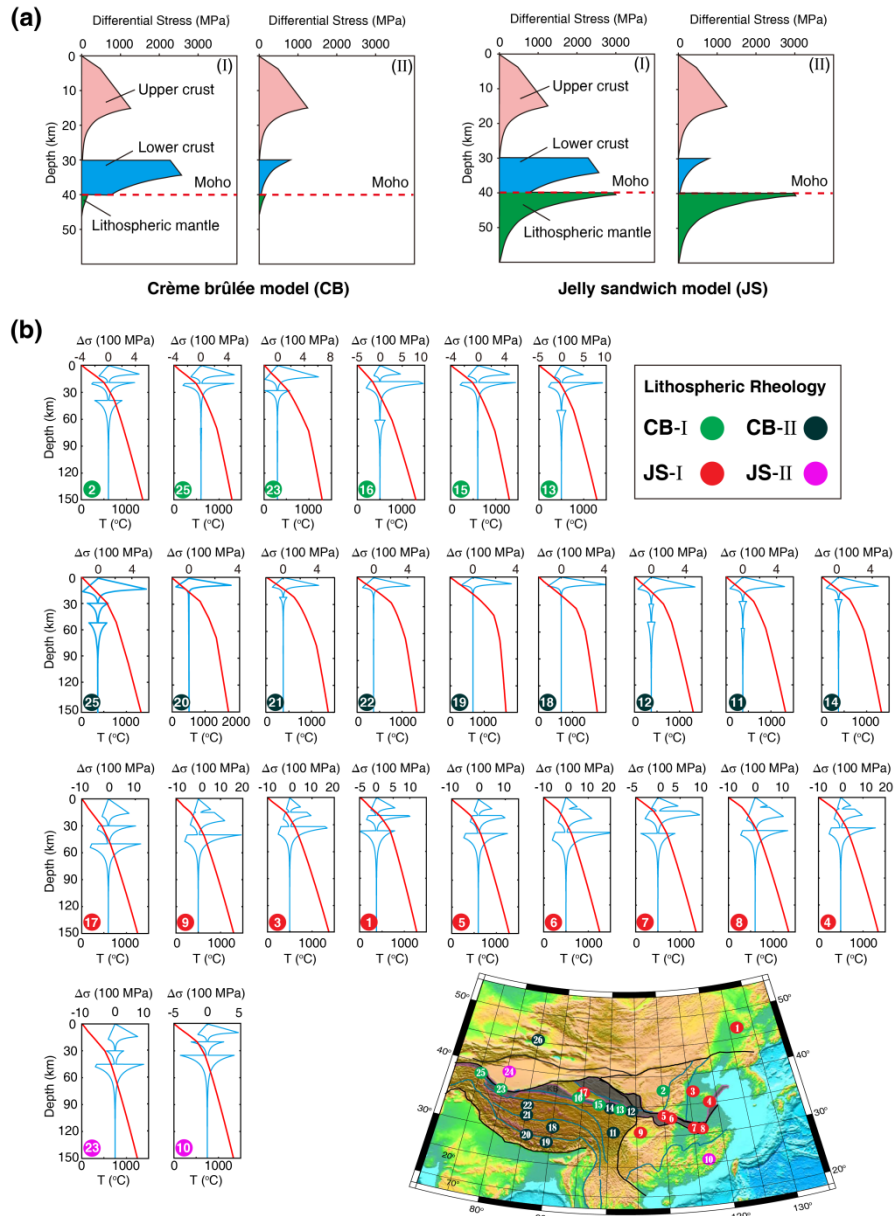
Figure 1. Four rheological models of continental lithosphere. (a) Crème brûlée model (CB) and Jelly sandwich model (JS). The two rheological models can be further subdivided into CB-I, CB-II, JS-I, and JS-II according to the strength of the lower crust (modified from Jackson, 2002). (b) Observations of four distinct lithosphere rheological structures implied for East Asia (modified from Zhang et al., 2013). Locations of strength profiles are pointed out by dots with numbers in the topography map. Dots filled with different colors indicate different models of lithospheric rheology. These strength profiles are calculated based on observed geothermal structure and lithospheric structure, and assumed that compositions of the upper and lower crust and lithospheric mantle are wet quartzite, undried granulite and dry olivine, respectively. ~~Here~~ Variations of temperature and ~~upper and lower crustal~~lithospheric compositions lead to a diverse suite of strength profiles vs. depth. ~~ORB: Ordos Basin; COB:~~
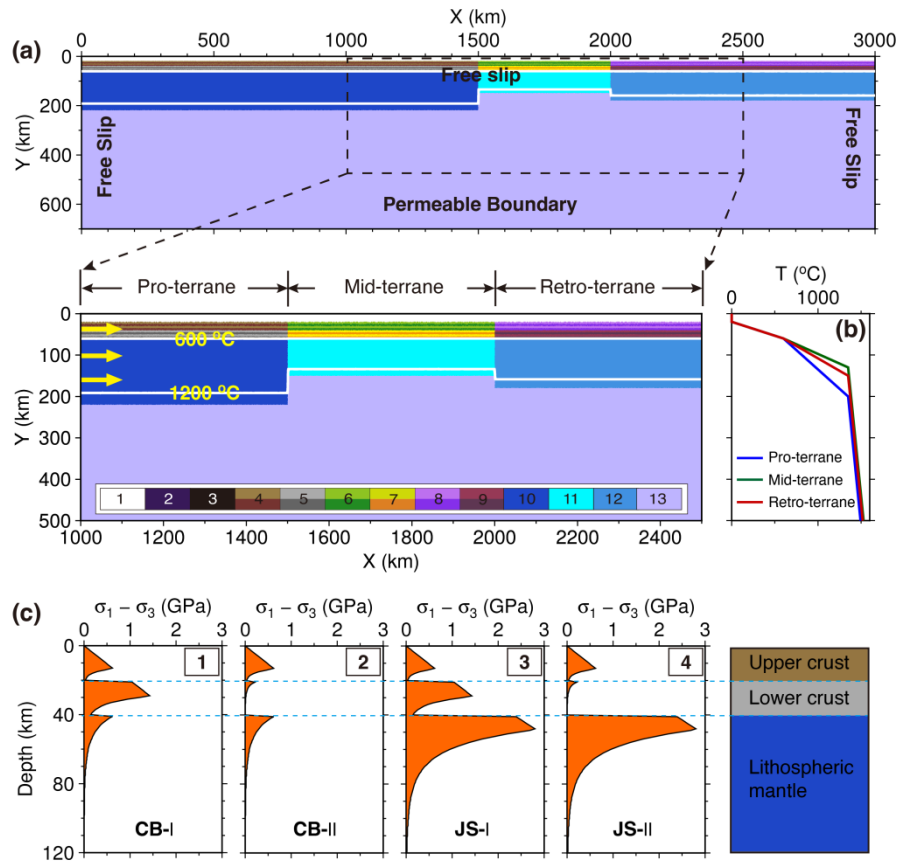
Figure 2. Initial model setup. (a) Initial model configuration. The model size is 3000 km × 700 km, and size of study region is 1500 km × 500 km. Three continental terranes of the Pro-, Mid- and Retro-terranes are contained in the numerical model, and they are 200 km, 130 km, and 160 km thick, respectively. White lines are isotherms with an interval of 600 ℃. Yellow arrows indicate the convergence rate of 20 mm/yr. Colored grids: 1 – sticky air; 2 – sediments; 3 – weak zone; 4, 6, 8 – the upper crust of the Pro-, Mid- and Retro-terranes, respectively; 5, 7, 9 – the lower crust of the Pro-, Mid- and Retro-terranes, respectively; 10, 11, 12 –lithospheric mantle of the Pro-, Mid- and Retro-terranes, respectively; 13 – asthenosphere. (b) Initial temperature structure for the three terranes. The Pro- and Mid-terranes respectively have a coldest and warmest lithospheric mantle due to their differences of lithosphere thicknesses. (c) Four rheological models with contrasting lithospheric strength profiles. These are derived from different strength scaling factor (S) combinations for the upper crust, lower crust, and lithospheric mantle (Table S1). Strength profiles are calculated based on the Pro-terrane's initial lithospheric structure, composition, and temperature field. The prescribed strain rate is 1×10^{-14} s^{-1}. CB-I and CB-II, the crème brûlée

700   model with strong and weak lower crust, respectively; JS-I and JS-II, the jelly sandwich model with strong and

701   weak lower crust, respectively.
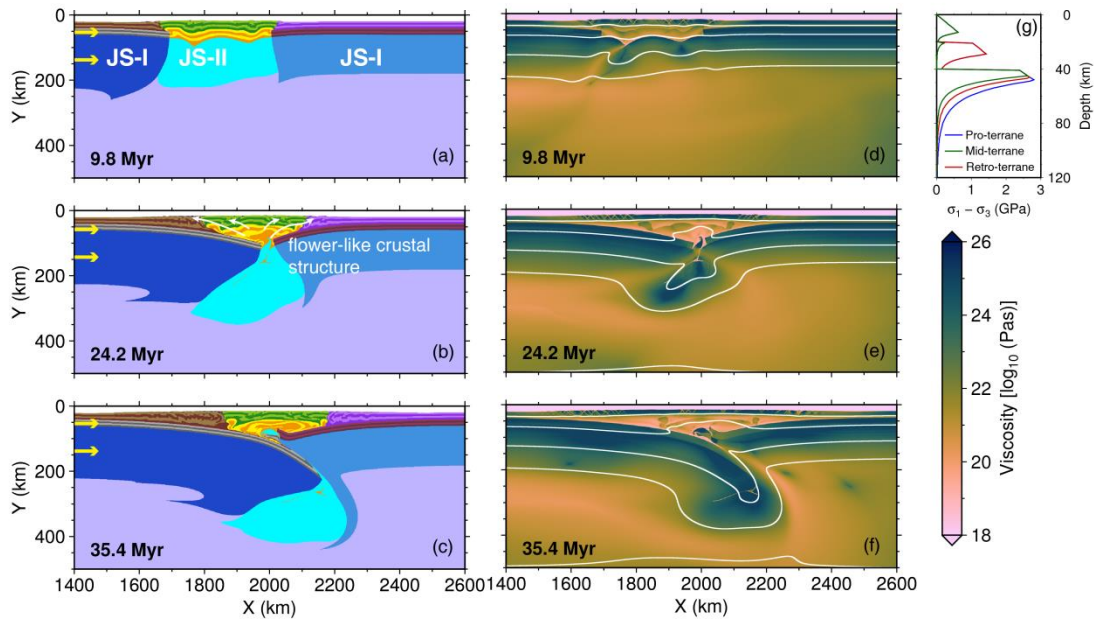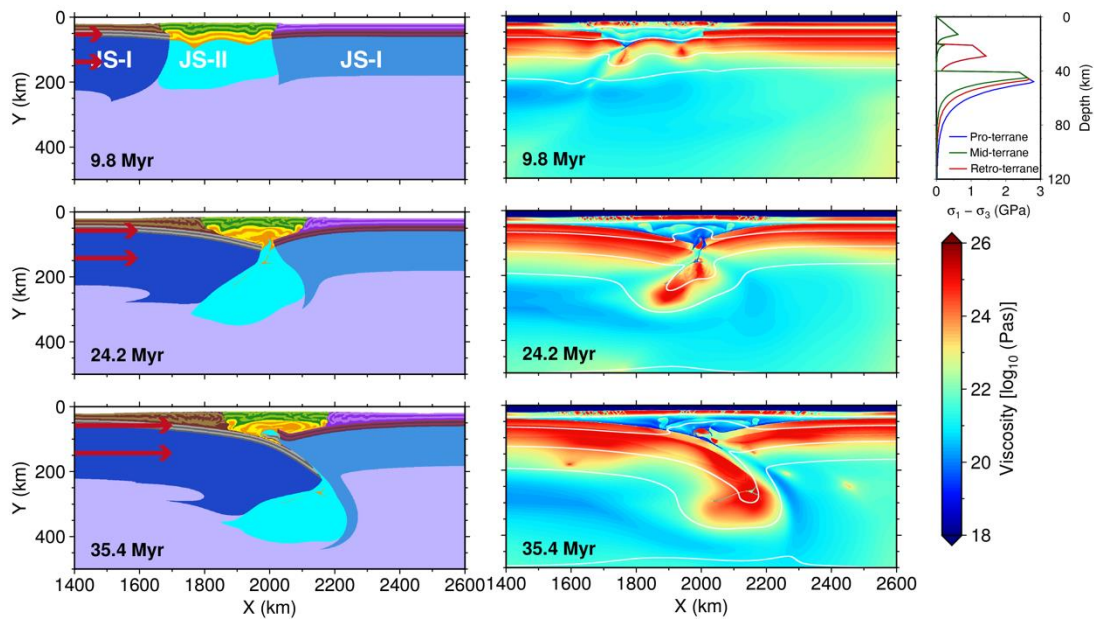
Figure 3. Collision of the lithospheres of the Pro- and Retro-terranes. Rheological models for the Pro-, Mid- and Retro-terranes are JS-I, JS-II, and JS-I, respectively, as shown in ~~the upper right corner~~(g). The left panel shows compositional fields at 9.8 Myr, 24.2 Myr, and 35.4 Myr, respectively. Yellow arrows indicate the convergence rate. The right panel shows the corresponding viscosities. White lines are isotherms with an interval of 300 °C.

710

711

712
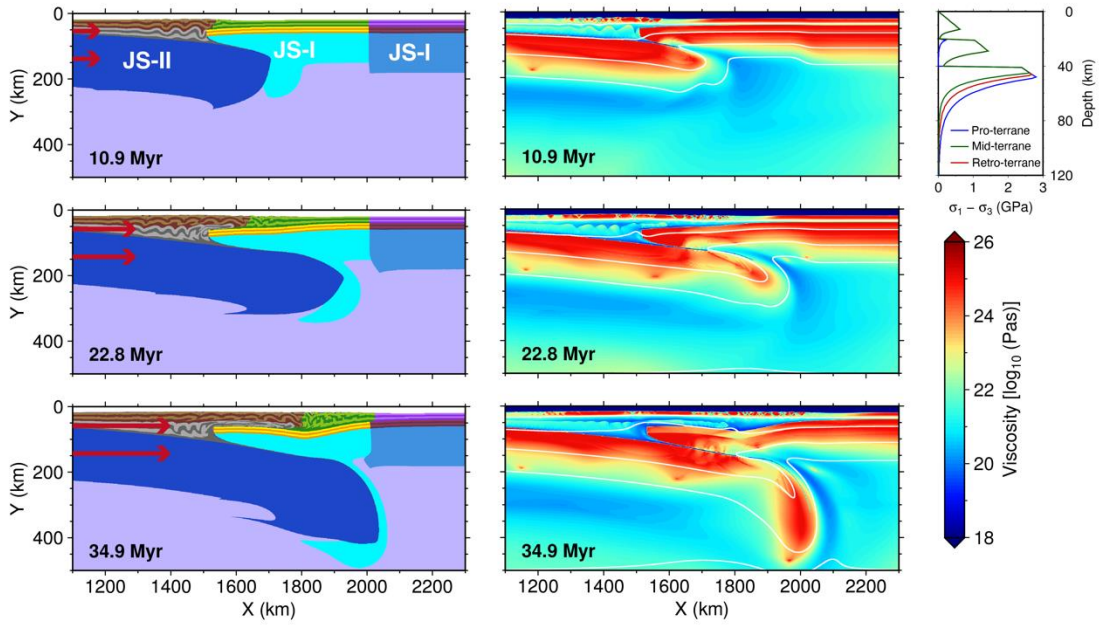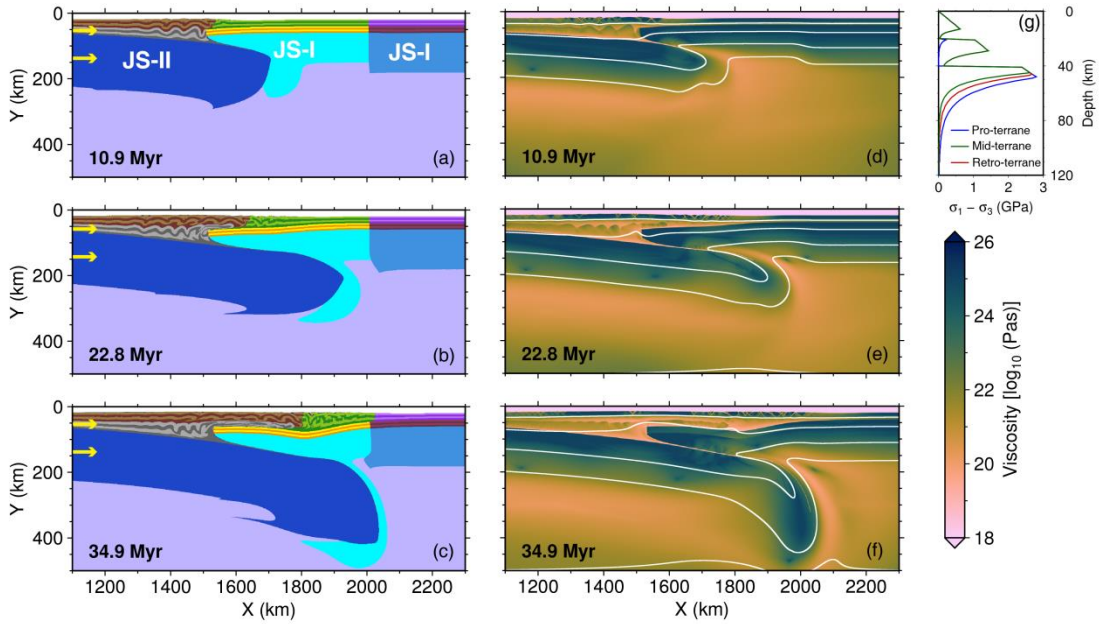
Figure 4. Subduction of the lithosphere of the Pro-terrane. Rheological models for the Pro-, Mid- and

Retro-terranes are JS-II, JS-I, and JS-I, respectively. See Figure 3 for plotting conventions.

715
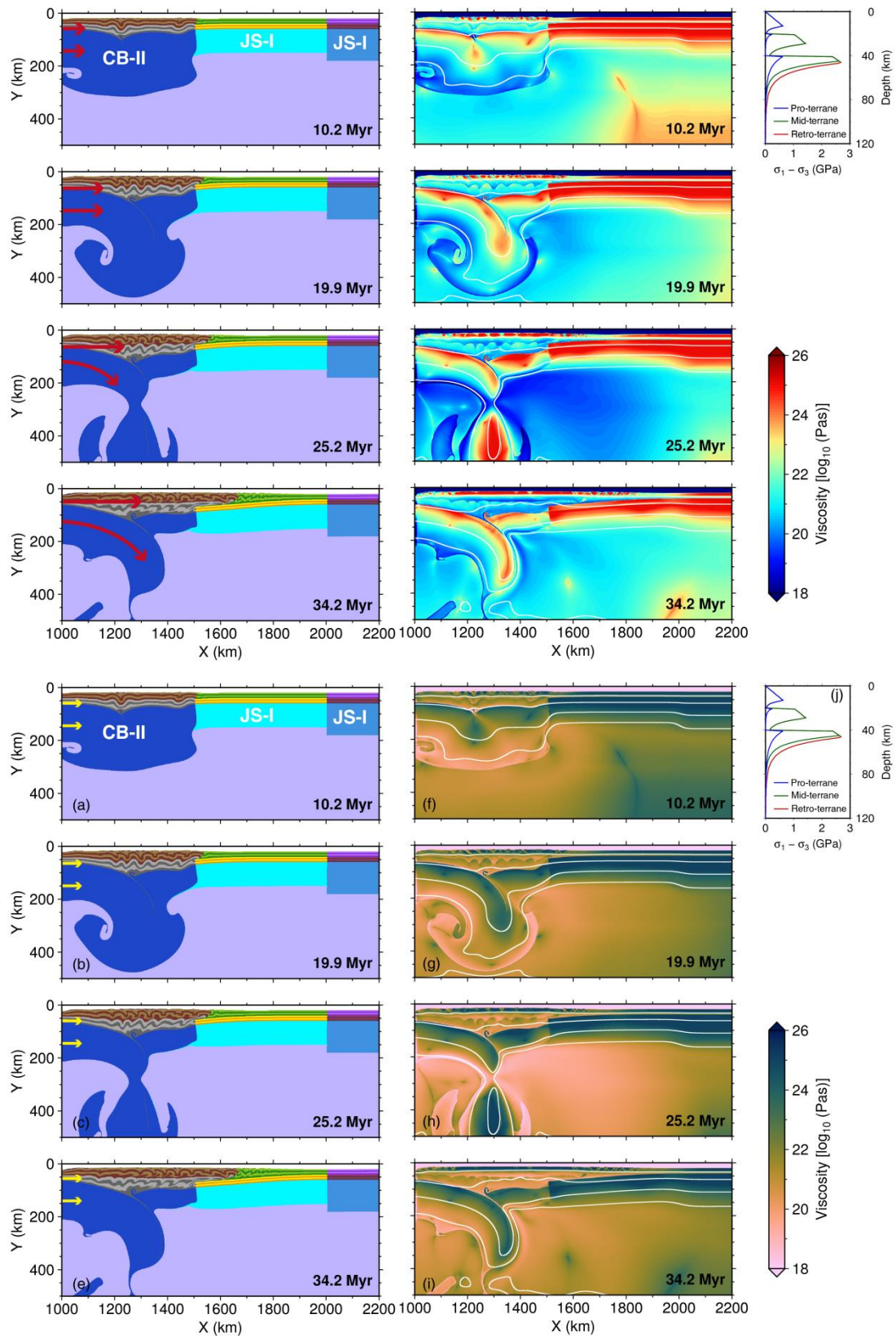
Figure 5. Thickening and delamination of the lithosphere of the Pro-terrane. Rheological models for the Pro-, Mid- and Retro-terranes are CB-II, JS-I, and JS-I, respectively. See Figure 3 for plotting conventions.
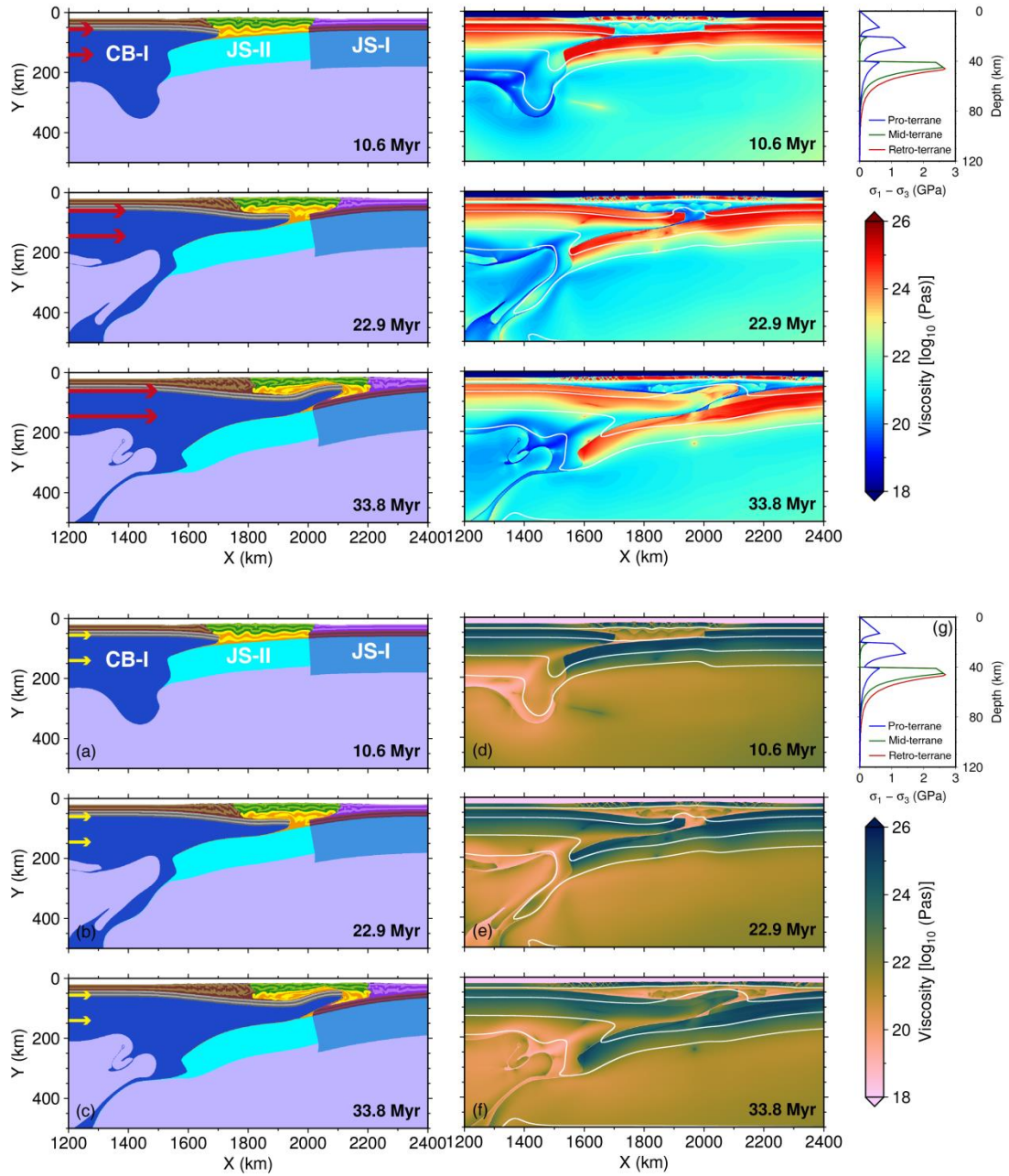
721

722

723 **Figure 6. Replacement of the lithosphere of the Pro-terrane.** Rheological models for the Pro-, Mid- and

724 Retro-terranes are CB-I, JS-II, and JS-I, respectively. See Figure 3 for plotting conventions.

725

726
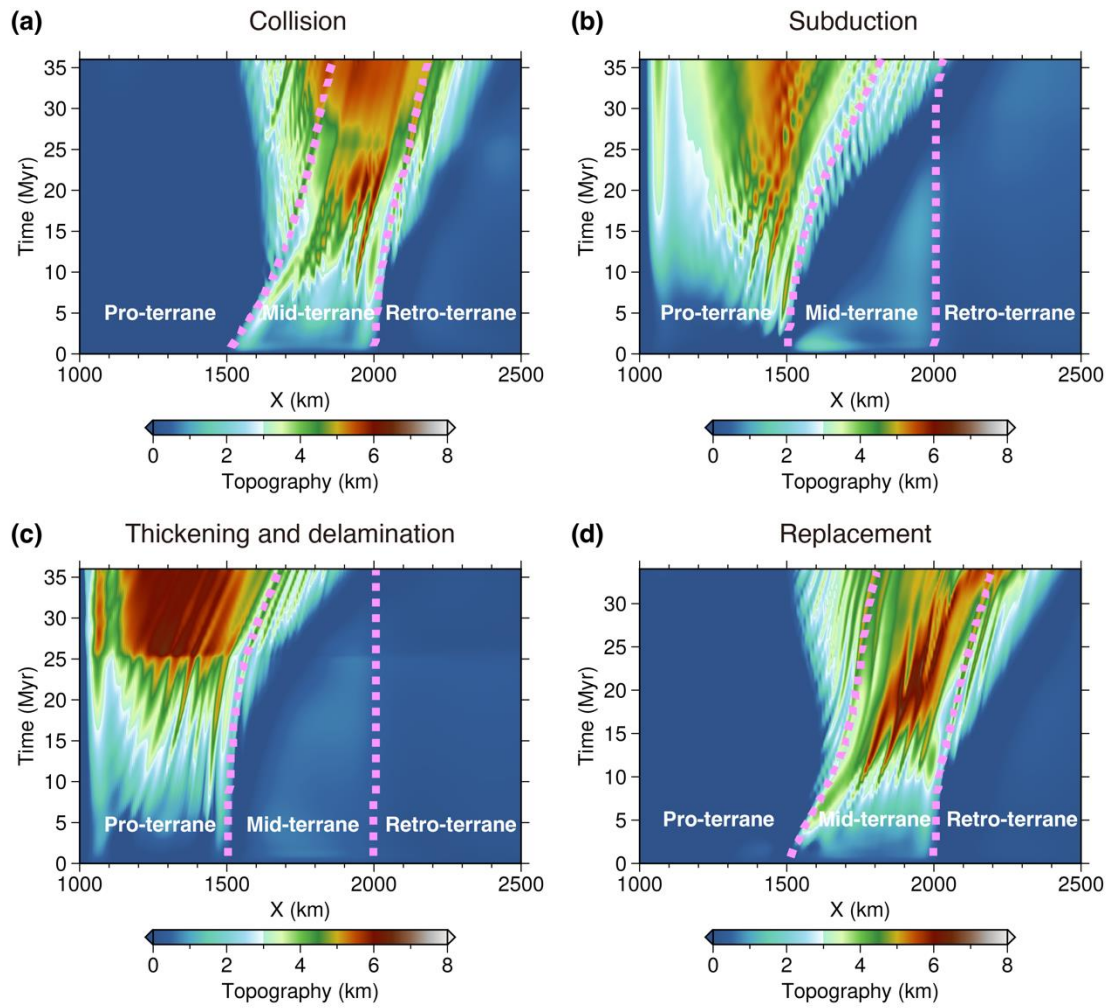
Figure 7. Evolution of surface relief for the different deformation styles. The purple dashed lines indicate the boundaries between terranes. (a) – (d) Surface relief associated with the deformation patterns of lithosphere collision, subduction, thickening and delamination, and replacement, respectively.

730

731

732
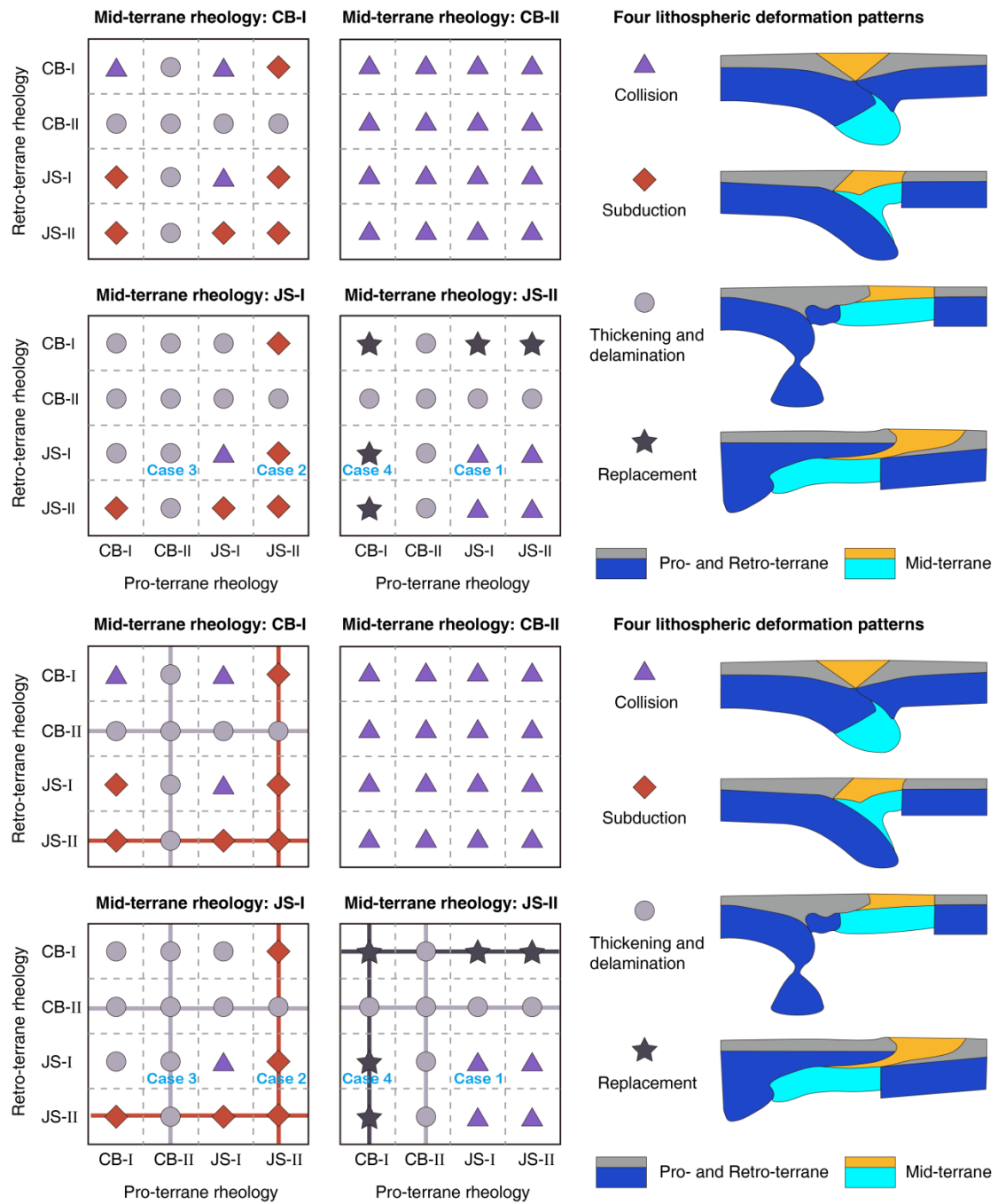
Figure 8. Four styles of lithosphere deformation patterns. Symbols with colors indicate different deformation patterns of the lithosphere. Cases 1 – 4 are the selected models chosen to illustrate details of these modes of compressional evolution.

733

734

735

736
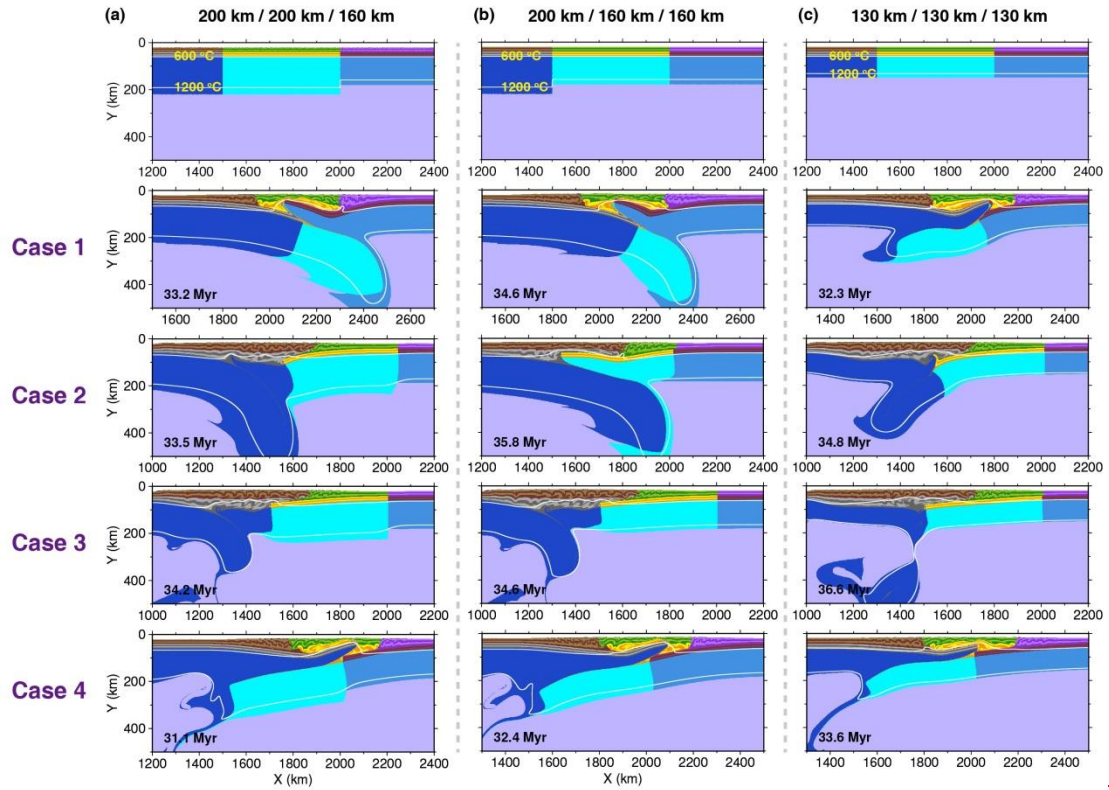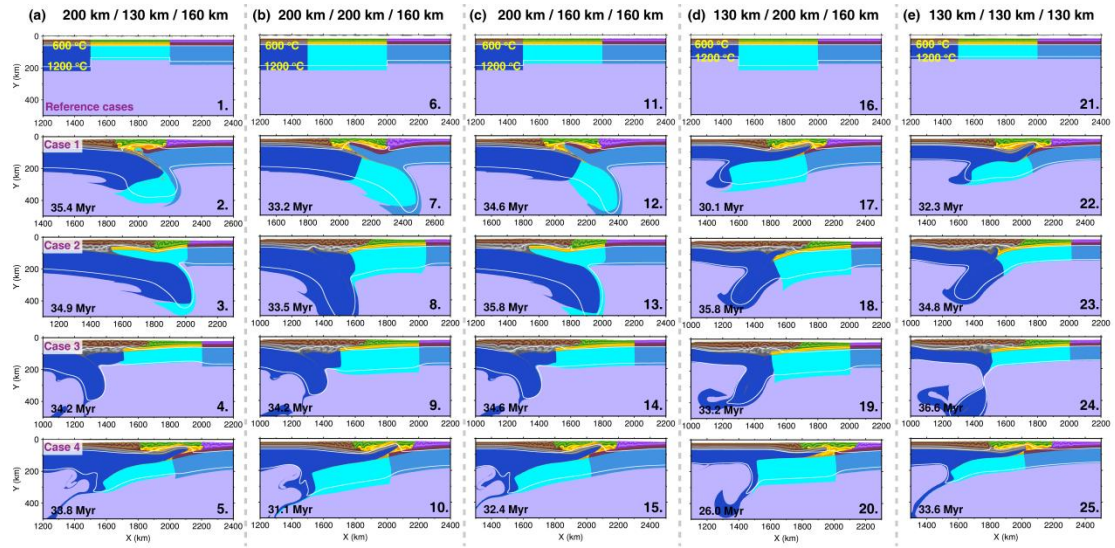
Figure 9. Effects of lithosphere thickness~~es~~ ~~variations between~~of various terranes. (a) – (~~e~~e) Final simulation results of models with the different ~~same~~ lithosphere thicknesses of the Pro-~~,~~ ~~and~~ Mid-~~,~~ and~~terranes, the Mid- and</u> Retro-terranes~~, and the Pro-, Mid- and Retro-terranes~~, respectively. (a) Final simulation results of reference cases. Rheological models of the Pro-, Mid- and Retro-terranes in 2 – 4 rows are same with those in Cases 1 – 4, respectively.
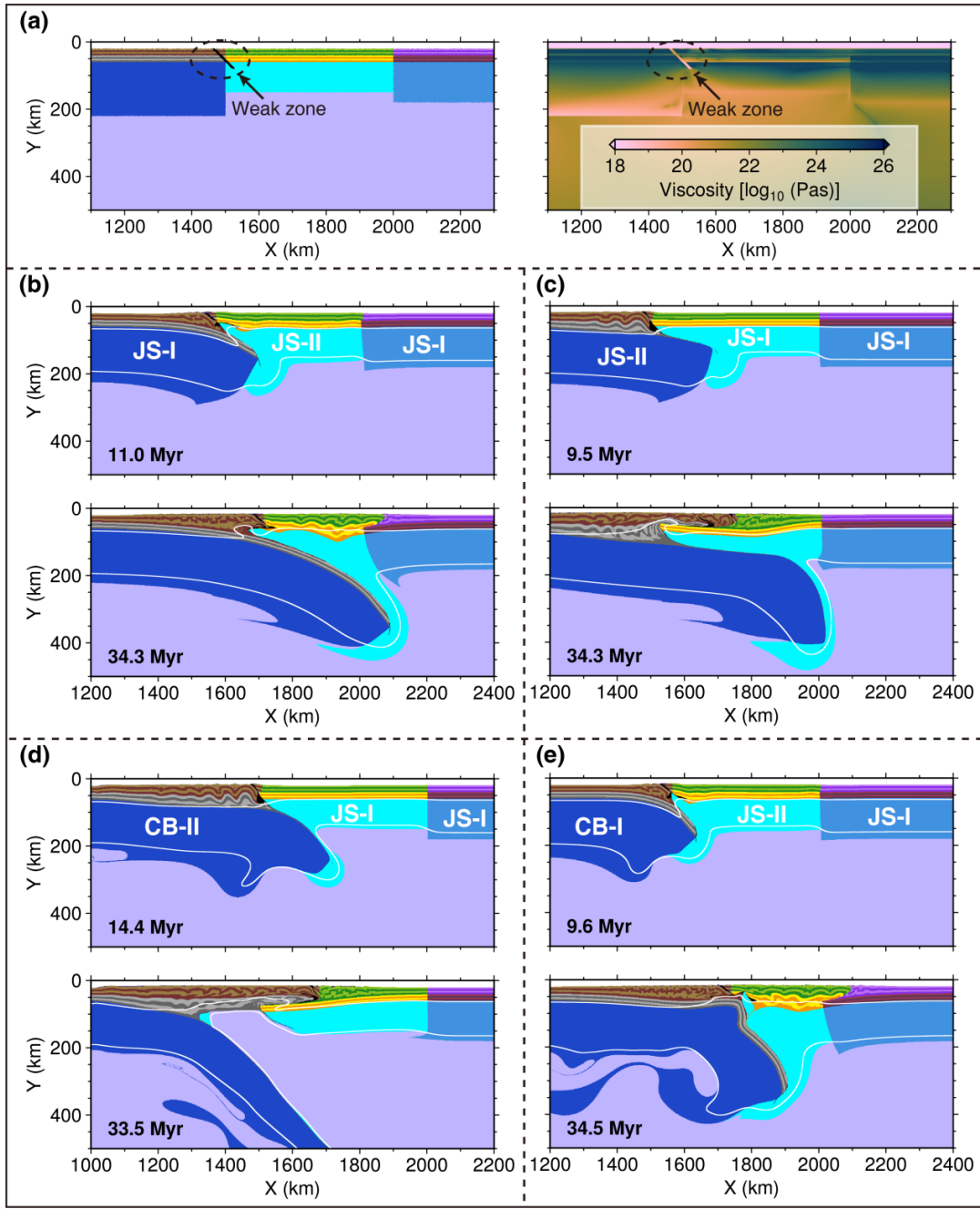
746

747 **Figure 10. Effects of local weak zone on lithosphere deformation.** (a) Details about the weak zone. (b) – (e)

748 Final simulation results of models corresponding to Cases 1 – 4, respectively.

749
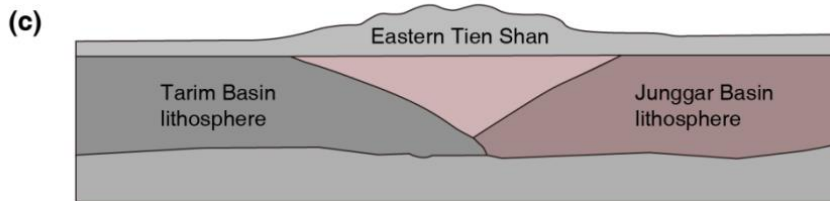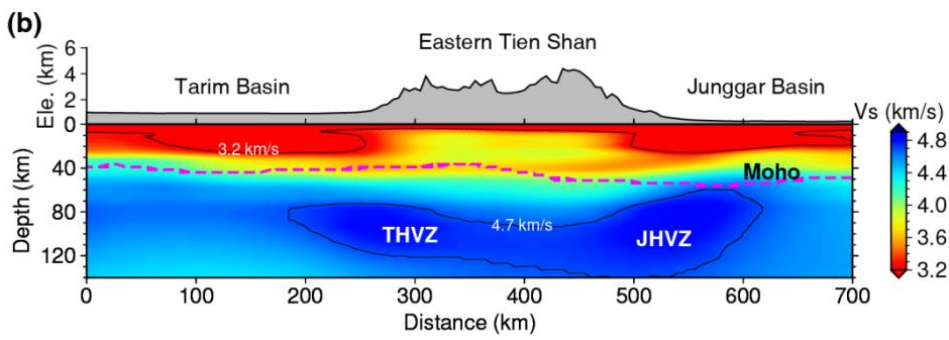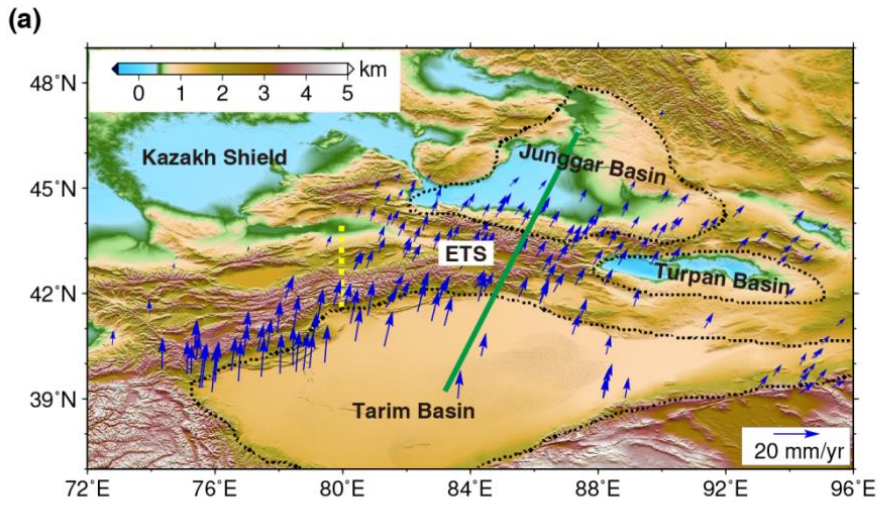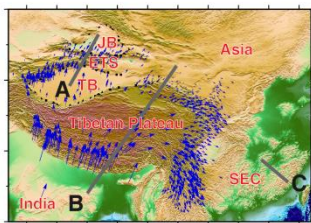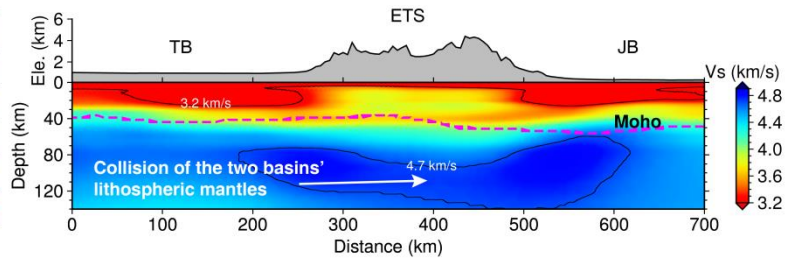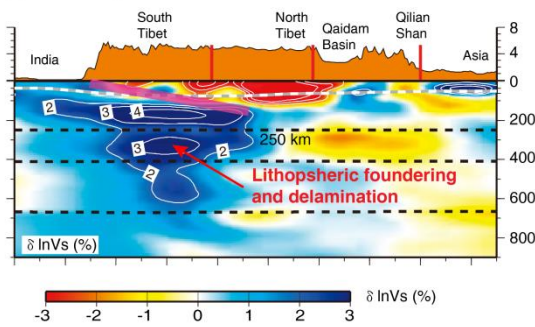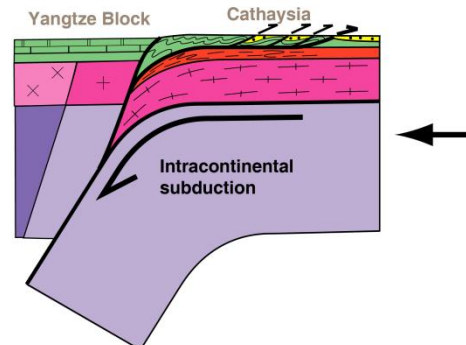
Figure ~~10~~11. Implications of simulation results to East Asia. (a) Topography of East Asia. The three gray lines point out the locations of lithosphere profiles in (b), (c) and (d). TB, Tarim Basin; ETS, eastern Tien Shan; JB, Junggar Basin; SEC, Southeastern China. (b) Collision of the lithospheric mantle of Tarim Basin and Junggar Basin beneath the eastern Tien Shan (modified from Lü et al., 2019). (c) Lithospheric founding and delamination in the Tibetan Plateau (modified from Chen et al., 2017). (d) Intracontinental subduction in the Early Paleozoic Orogen in southeastern China (modified from Faure et al., 2009). ~~Lithosphere structure of the eastern Tien Shan. (a) Topography and crustal movement of the eastern Tien Shan and its surrounding areas. Arrows indicate GPS velocities (Wang and Shen, 2020). The yellow dashed line shows the boundary of geographic longitude of 80° E. (b), (c) Vs velocities and lithosphere structure across the Tarim Basim, eastern Tien Shan, and the Junggar Basin (modified from Lü et al., 2019). ETS, eastern Tien Shan; THVZ, Tarim Basin high-velocity zone; JHVZ, Junggar Basin high-velocity zone.~~

764   **Table 1. Flow laws and material properties for different lithospheric layers.** ρ_0 is the initial density; it evolves

765   with time as $\rho = \rho_0 \left(1 - \alpha (T - T_0)\right)\left(1 + \beta (P - P_0)\right)$, where $T_0 = 20\,°C$, $P_0 = 10^5$ MPa. Flow law: qtz. = quartzite, Plag.

766   = plagioclase, ol. = olivine.

Material properties	Sediment	Upper crust	Lower crust	Lithospheric mantle	Asthenosphere
ρ_0 (kg/m^3)	2600	2700	2800	3300	3300
Flow laws	Wet qtz.	Wet qtz.	Plag.	Dry ol.	Dry ol.
$1/A_D$ (Pa^n s)	1.97×10^{17}	1.97×10^{17}	4.80×10^{22}	3.98×10^{16}	3.98×10^{16}
n	2.3	2.3	3.2	3.5	3.5
E_a (KJ/mol)	154	154	238	532	532
V_a (J/bar)	0.8	0.8	1.2	1.2	1.2
$\phi = sin(\varphi)$	0.2 – 0.1	0.3 – 0.1	0.3 – 0.1	0.6 – 0.4	0.6 – 0.3
C (Pa)	$1 \times 10^{7\text{-}6}$	$1 \times 10^{7\text{-}6}$	$1 \times 10^{7\text{-}6}$	$1 \times 10^{7\text{-}6}$	$1 \times 10^{7\text{-}6}$
H_r (uW/m^3)	2.0	1.5	0.5	0.022	0.022
C_p (J/kg K)	1000	1000	1000	1000	1000
α (1/K)	3×10^{-5}	3×10^{-5}	3×10^{-5}	3×10^{-5}	3×10^{-5}
β (1/MPa)	1×10^{-5}	1×10^{-5}	1×10^{-5}	1×10^{-5}	1×10^{-5}
k (W/m/K)	$0.64 + 807/(T+77)$	$0.64 + 807/(T+77)$	$1.18 + 474/(T+77)$	$[0.73 + 1293/(T+77)] \times (1 + 0.00004P)$	$[0.73 + 1293/(T+77)] \times (1 + 0.00004)$

767